

## MATERIALS SCIENCE

# Microfluidic bioprinting of tough hydrogel-based vascular conduits for functional blood vessels

Di Wang<sup>1,2†</sup>, Sushila Maharjan<sup>1†</sup>, Xiao Kuang<sup>1†</sup>, Zixuan Wang<sup>1</sup>, Luis S. Mille<sup>1</sup>, Ming Tao<sup>3</sup>, Peng Yu<sup>3</sup>, Xia Cao<sup>1</sup>, Liming Lian<sup>1</sup>, Li Lv<sup>1</sup>, Jacqueline Jialu He<sup>1</sup>, Guosheng Tang<sup>1</sup>, Hyunwoo Yuk<sup>4</sup>, C. Keith Ozaki<sup>3\*</sup>, Xuanhe Zhao<sup>4,5\*</sup>, Yu Shrike Zhang<sup>1\*</sup>

Three-dimensional (3D) bioprinting of vascular tissues that are mechanically and functionally comparable to their native counterparts is an unmet challenge. Here, we developed a tough double-network hydrogel (bio)ink for microfluidic (bio)printing of mono- and dual-layered hollow conduits to recreate vein- and artery-like tissues, respectively. The tough hydrogel consisted of energy-dissipative ionically cross-linked alginate and elastic enzyme-cross-linked gelatin. The 3D bioprinted venous and arterial conduits exhibited key functionalities of respective vessels including relevant mechanical properties, perfusability, barrier performance, expressions of specific markers, and susceptibility to severe acute respiratory syndrome coronavirus 2 pseudo-viral infection. Notably, the arterial conduits revealed physiological vasoconstriction and vasodilatation responses. We further explored the feasibility of these conduits for vascular anastomosis. Together, our study presents biofabrication of mechanically and functionally relevant vascular conduits, showcasing their potentials as vascular models for disease studies *in vitro* and as grafts for vascular surgeries *in vivo*, possibly serving broad biomedical applications in the future.

## INTRODUCTION

The blood vessels are responsible for transporting blood cells, nutrients, and oxygen to the tissues of the human body and for taking carbon dioxide and other wastes away. In terms of anatomical structures and functions, there are three main types of blood vessels: arteries, veins, and capillaries. While a capillary consists of only a layer of endothelial cells (ECs) supported by the subendothelial basement membrane and connective tissue, both arteries and veins have three concentric layers, *i.e.*, tunica intima, tunica media, and tunica externa. Tunica intima is the innermost and thinnest layer and is mainly made up of ECs, which play pivotal roles in regulating coagulation, conferring selective permeability, and participating in transendothelial migration of circulating cells (1, 2). Tunica media, the middle layer, mainly consisting of smooth muscles, especially in the veins and smaller arteries, controls the vessel's caliber and withstands blood pressures. In the arteries, tunica medium becomes the thickest layer among the three, but in the veins, it is obviously thinner. Tunica externa, principally composed of connective tissues, serves as the outer layer (3).

Cardiovascular diseases, such as ischemic heart disease, cerebellar stroke, and venous thrombosis, remain the leading causes of mortality and disability of human. Total prevalent cases doubled from 271 million in 1990 to 523 million in 2019, and the number of deaths kept increasing from 12.1 million to 18.6 million in the past 30 years (4–6). Revascularization is commonly achieved by bypass

surgeries based on the grafting of autologous veins (*e.g.*, the saphenous veins) and arteries (*e.g.*, the internal mammary arteries), and these expensive procedures are performed more than 400,000 times annually in the United States alone (7, 8). However, autologous grafts for the heart and extremities have several drawbacks; specifically, the long-term patency rates remain low (9, 10), and donor-site injuries caused by invasive harvesting remain morbid for patients (11). Graft failure is largely driven by intimal hyperplasia and atherosclerosis (12, 13). As an alternative to autologous grafts, synthetic grafts, first introduced in the 1950s, made from poly(ethylene terephthalate) and expanded polytetrafluoroethylene, have been widely used (14). However, small caliber synthetic grafts suffer from high rates of failure due to thrombogenicity, accelerated intimal hyperplasia at the distal anastomosis, and infectious complications (15). The patency rates of synthetic substitutes are even lower than those of autologous grafts, where only 50% of synthetic grafts would survive 2 years in the peripheral circulation (10).

To overcome the limitations of autologous and conventional synthetic vascular grafts, various tissue-engineering strategies, including three-dimensional (3D) bioprinting, have emerged as potential vascular tissue-engineering approaches for fabricating viable vascular conduits. 3D bioprinting allows the recreation of vascular structures by precisely positioning biomaterials, cells, and possibly biologic signaling molecules (such as growth factors) to mimic their anatomical characteristics and facilitate tissue regeneration (16, 17). Numerous bioprinting techniques, including extrusion-, inkjet-, and laser-based bioprinting, have been rapidly developed and applied in bioprinting of vascularized tissue constructs and perfusable vascular structures (18). In particular, a variation of extrusion-based bioprinting method, termed microfluidic coaxial bioprinting, can simultaneously deliver the bioink and the cross-linking agents as separate flow streams through a concentric nozzle, which allows single-step generation of stand-alone, hollow vascular conduits (19–21). A wide range of sizes of the resulting vascular conduits with varying performances is conveniently attainable through microfluidic coaxial

<sup>1</sup>Division of Engineering in Medicine, Department of Medicine, Brigham and Women's Hospital, Harvard Medical School, Cambridge, MA 02139, USA. <sup>2</sup>Plastic Surgery Hospital, Chinese Academy of Medical Sciences and Peking Union Medical College, Beijing 100144, P. R. China. <sup>3</sup>Department of Surgery and the Heart and Vascular Center, Brigham and Women's Hospital, Harvard Medical School, Boston, MA 02115, USA. <sup>4</sup>Department of Mechanical Engineering, Massachusetts Institute of Technology, Cambridge, MA 02139, USA. <sup>5</sup>Department of Civil and Environmental Engineering, Massachusetts Institute of Technology, Cambridge, MA 02139, USA. \*Corresponding author. Email: yszhang@research.bwh.harvard.edu (Y.S.Z.); zhaox@mit.edu (X.Z.); ckozaki1@bwh.harvard.edu (C.K.O.) †These authors contributed equally to this work.

bioprinting using different nozzle setups and bioink designs. For example, Hong *et al.* (22) successfully adopted a quick-gelling bioink to bioprint perfusable vessels. Andrique *et al.* (23) developed functional vesseloids with vasoactivities and permeability. Gao *et al.* (24, 25) reported tunable vascular equivalents containing endothelium by cell-laden alginate and extracellular matrix-based bioink as in vitro models. We also reported the bioprinting of cell-laden hollow fibers facilitating the proliferation and maturation of vascular cells (26), which could be further expanded to the engineering of cannular tissues of multiple circumferential layers (27), offering an approach for biofabrication of vascular conduits with different anatomical features.

Nevertheless, in many cases, including previous works of our own, these bioprinted vascular conduits only partially recapitulated the structural and functional features of the native blood vessels. These vascular conduits had substantially weaker mechanical strengths than their native counterparts, limiting their biological applications under a physiological environment. Some other reports focused on developing synthetic polymer-based hybrid hydrogels, including nanocomposite hydrogels and double-network (DN) hydrogels that convey high strengths and toughness (28, 29), which laid a foundation for bioprinting of mechanical robust tubular structures. Although these synthetic polymer-based hydrogels are mechanically strong and cytocompatible, they may not support the spreading and proliferation of the embedded cells, limiting their desired biofunctions. Therefore, it remains a challenge to bioprint structurally similar, mechanically, and functionally relevant vascular conduits, particularly those serving as small-diameter vascular grafts.

Here, we present a stretchable DN hydrogel (bio)ink system for microfluidic bioprinting of small-diameter vascular conduits that favorably recapitulated structural and biological functions of their native counterparts. The (bio)ink prepolymer, composed of sodium alginate and gelatin [or gelatin methacryloyl (GelMA)], was cross-linked by calcium chloride ( $\text{CaCl}_2$ ) and microbial transglutaminase (mTG), respectively, generating a DN hydrogel with excellent mechanical properties and good biocompatibility. Using microfluidic bioprinting, two distinct approaches were adopted to fabricate venous and arterial engineered vessels closely resembling their native counterparts. Specifically, venous conduits were generated by (bio)printing monolayered hydrogel tubes, followed by seeding human umbilical vein ECs (HUVECs) in the lumens and human umbilical vein smooth muscle cells (HUVSMCs) on the outer surfaces. In contrast, arterial conduits were generated by direct bioprinting of the outer human umbilical artery SMC (HUASMC)-encapsulated layer and inner hydrogel layer, followed by seeding human umbilical artery ECs (HUAECs) in the lumens. Both venous and arterial conduits exhibited key properties of blood vessels, including high stretchability, apparent perfusability, and barrier performance. The arterial conduits displayed constriction and dilation responses to vasoconstrictor and vasodilator, respectively. Furthermore, we demonstrated the applicability of these vascular conduits for studying diseases and drug testing in vitro, by infecting them with pseudotyped severe acute respiratory syndrome coronavirus 2 (SARS-CoV-2) viral particles (pCoV-VPs) expressing spike proteins and subjecting them to treatment with antiviral drugs. Similarly, we conducted ex vivo vascular anastomoses by connecting the vascular conduits with a human popliteal vein or a mouse aorta, as well as preliminary in vivo vascular anastomosis with a mouse vena cava, illustrating the potential of the 3D (bio)printed vascular conduits as vascular grafts in the future.

## RESULTS AND DISCUSSION

### Design and mechanics of tough DN hydrogels

Central to the (bio)printing of biomimetic vessels is to develop a cytocompatible (bio)ink with suitable rheological properties, cell-benign cross-linking, and vessel-relevant mechanical performances. Tough hydrogels that have excellent mechanical properties are highly desired for such a purpose. Recent advances in DN hydrogels provide a general method to fabricate hydrogel constructs with unprecedented mechanical properties and good biocompatibility (30, 31). With these in mind, we engineered a set of natural polymer-based DN hydrogels consisting of alginate physically cross-linked by calcium and gelatin covalently cross-linked by mTG (Fig. 1A). Gelatin can form covalent cross-links between glutamine and lysine groups upon treatment with mTG and intrinsically has arginylglycylaspartic acid (ArgGlyAsp or RGD) peptide sequences that promote cell adhesion and proliferation (32). Note that mTG is a U.S. Food and Drug Administration-approved enzyme to achieve cell-benign cross-linking (33). The ionically cross-linked alginate, also biocompatible, enables effective energy dissipation for enhancement of mechanical properties (30, 34). Besides the excellent biocompatibility, another prominent advantage of using these natural polymers is the existence of electrostatic interactions within the selected components, enabling tunable rheological properties of the bioink. For example, for the hybrid (bio)ink containing 1% medium viscosity alginate (MAlg) and 15% gelatin (MAlgGel15) in distilled water, alginate exhibits a net negative charges, and gelatin polyanpholyte has a net positive charge at pH 5.5 (below gelatin's isoelectric point), leading to the formation of a soluble complex by electrostatic attraction. The strong electrostatic interactions between alginate and gelatin were validated by a high apparent viscosity (7 Pa-s), which was more than 40 times higher than those of the individual components (approximately 0.14 to 0.17 Pa-s) at the shear rate of  $0.1 \text{ s}^{-1}$  at  $37^\circ\text{C}$  (Fig. 1B).

The mechanics of the DN hydrogels were studied by tensile tests. We first investigated the mechanical properties of the individual components. Figure 1C shows the loading-unloading stress-strain curves of the 1% MAlg (MAlg1) hydrogel and the 15% gelatin (Gel15) hydrogel separately, as well as the hybrid (bio)ink containing these two components together (MAlg1Gel15), to a maximum strain of 25%. The MAlg hydrogel physically cross-linked by 2%  $\text{CaCl}_2$  and the gelatin hydrogel covalently cross-linked by 2% mTG showed moduli of 242.1 and 34.6 kPa, respectively (fig. S1A). The physically cross-linked alginate exhibited a large hysteresis ratio (78%) and a large irreversible strain (22%). Although the gelatin hydrogel showed a low hysteresis ratio of 9% and a low strain set (1%), its mechanical property was weak because of the lack of energy dissipation. The MAlg1Gel15 hydrogel, cross-linked with 2%  $\text{CaCl}_2$  and 2% mTG ( $\text{CaCl}_2/\text{mTG}$ ), exhibited a lower Young's modulus (142.8 kPa) than that of the pure MAlg1 hydrogel (fig. S1A), likely attributed to the suppression of alginate cross-linking by the electrostatic interactions between alginate and gelatin chains. The MAlg1Gel15 DN hydrogel had higher strength and stretchability than those of single-component hydrogels due to the two intertwined networks (fig. S1B). The physically cross-linked alginate network tremendously contributed to energy dissipation in the DN hydrogel, as indicated by the hysteresis ratio of 49% (fig. S1C). The DN hydrogel also showed a low irreversible strain or strain set (5%) during loading-unloading cycles using a maximum strain of 25% (fig. S1D), due to the covalently cross-linked gelatin network. These results confirmed that the alginate-gelatin hydrogel is a DN hydrogel with enhanced mechanical performance.

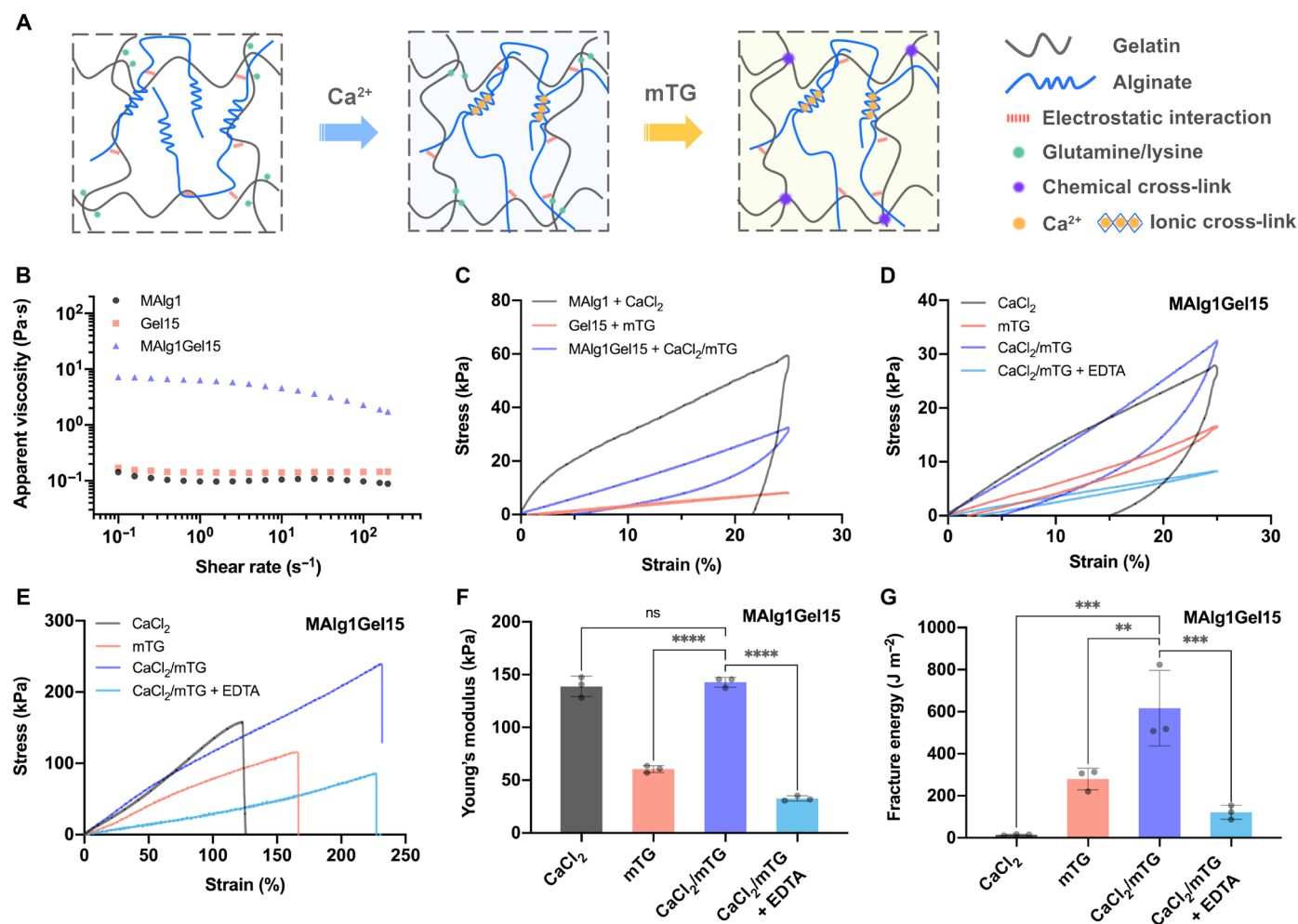


**Fig. 1. Design and mechanical properties of tough DN hydrogel (bio)inks.** (A) Schematics of DN hydrogel containing physically cross-linked alginate by calcium as the first network and chemically cross-linked gelatin by mTG as the second network. (B) Apparent viscosities as a function of shear rate for (bio)ink (MAIg1Gel15) and its individual components (MAIg1 and Gel15) at 37°C. (C) Loading-unloading tensile stress-strain curves of MAIg1, Gel15, and MAIg1Gel15 hydrogels cross-linked by CaCl<sub>2</sub>, mTG, and CaCl<sub>2</sub>/mTG, respectively. The maximum strain was 25%. (D) Loading-unloading tensile stress-strain curves of the MAIg1Gel15 hydrogels with four different cross-linking and posttreatment methods: CaCl<sub>2</sub>, mTG, CaCl<sub>2</sub>/mTG, and CaCl<sub>2</sub>/mTG/EDTA. The maximum strain was 25%. Tensile stress-strain curves (E), Young's moduli (F), and fracture energies (G) of MAIg1Gel15 hydrogels with four different cross-linking and posttreatment methods: CaCl<sub>2</sub>, mTG, CaCl<sub>2</sub>/mTG, and CaCl<sub>2</sub>/mTG/EDTA. ns, no significant difference. \*\**P* < 0.01, \*\*\**P* < 0.001, and \*\*\*\**P* < 0.0001.

We further analyzed the role of physical and chemical cross-linking in the mechanical properties of DN hydrogels. The DN hydrogels with physical, chemical, and dual cross-linking were fabricated. To decouple the contributions of physical and chemical cross-linking, a chelating agent, EDTA, was used to selectively cleave the physical cross-linking in the DN hydrogels. As shown in Fig. 1D, the dual cross-linked DN hydrogel manifested lower energy dissipation (smaller hysteresis loop) and higher strain recovery than those of hydrogels having only physical cross-linking. The hydrogel with only chemical cross-linking by mTG also exhibited an obvious hysteresis loop (hysteresis ratio of 20%; fig. S2A), due to energy dissipation by electrostatic interactions between alginate and gelatin. In the dual-cross-linked DN hydrogel, the electrostatic interactions could provide physical anchoring between the dense physical network and the loose covalent network, facilitating stress-transfer and additional energy dissipation. Therefore, the dual cross-linked DN hydrogels had

the highest tensile strength (197.7 kPa) and tensile strain (207.3%) compared with the single-network hybrid hydrogels (Fig. 1E). Compared with conventional DN hydrogels with independent cross-linking of each component, the ionic cross-linking and enzymatic cross-linking in our design could influence each other in the resulting DN hydrogel, as indicated by the similar modulus of the DN hydrogel to that of the hydrogel with only ionic cross-linking (Fig. 1F). This result was also supported by the lower Young's modulus of the EDTA-treated hydrogels than that of hydrogels only cross-linked by mTG, because the fast and dense ionic cross-linking of alginate could likely decrease the enzymatic cross-linking degree of gelatin because of high network-hindrance (35).

Owing to effective energy dissipation and enhanced stretchability, the dual cross-linked DN hydrogel offered a high toughness of 616.3 J m<sup>-2</sup>, exceeding that of the physically cross-linked single-network hydrogel (14.9 J m<sup>-2</sup>) and the chemically cross-linked

single-network hydrogel ( $279.5 \text{ J m}^{-2}$ ; Fig. 1G). After removal of the physical network of the DN hydrogel by EDTA, the fracture energy reduced to merely  $121.5 \text{ J m}^{-2}$ , highlighting the crucial role of the alginate physical network in energy dissipation in the tough DN hydrogels. Although the alginate network can be damaged during deformation, the stretchy gelatin network would maintain the material integrity (fig. S2B).

### Microfluidic coaxial extrusion (bio)printing and mechanical properties of (bio)printed vascular conduits

After understanding the mechanical properties, the tough DN hydrogel (bio)inks were used for the high-throughput fabrication of vascular conduits by coaxial extrusion (bio)printing. Two types of multichannel coaxial extrusion systems featuring two or three channels were used to produce monolayered or dual-layered vascular conduits, respectively (fig. S3).  $\text{CaCl}_2$  solution flowing in the core layer acted as the physical cross-linker for alginate in the hybrid (bio)ink (Fig. 2A). The (bio)printed conduits were subsequently treated with the  $\text{CaCl}_2/\text{mTG}$  solution for postprinting curing. (Bio)inks with different formulations were exploited to (bio)print tubes with widely tunable mechanical properties. Before setting the (bio)printing parameters, the rheological properties of two typical (bio)inks were measured. In Fig. 2B, the complex viscosity of the (bio)ink MALg1Gel15 decreased two orders of magnitude with a transition temperature at approximately  $31^\circ\text{C}$ . Above the transition temperature, the (bio)ink transformed from solid to liquid, as indicated by the plateau loss modulus exceeding the storage modulus (fig. S4A). At a lower temperature (such as  $30^\circ\text{C}$ ), the viscosity and shear stress of the MALg1Gel15 (bio)ink became very high and thus not suitable for microfluidic extrusion (bio)printing (fig. S4, B and C). Meanwhile, another DN hydrogel (bio)ink containing 2% low-viscosity alginate (LAlg) and 3% GelMA (LAlg2GM3), which was found to be suitable for cell encapsulation, was also measured. LAlg2GM3 had a much higher viscosity than individual components, again due to the electrostatic interactions between the components (fig. S4D). However, its viscosity was very low at both room temperature and  $37^\circ\text{C}$  because of the relatively low polymer concentration and weak electrostatic interactions between alginate and GelMA (fig. S4, E and F).

The rheological properties of various (bio)inks could be fine-tuned to facilitate coaxial extrusion (bio)printing by adjusting the temperature. For example, the MALg1Gel15 (bio)ink with a transition temperature of  $31^\circ\text{C}$  could be heated to  $37^\circ\text{C}$ , yielding a low-viscosity fluid (Fig. 2C). In comparison, the LAlg2GM3 (bio)ink needed to be cooled down to increase the viscosity and impart shear-thinning for (bio)printing at room temperature (fig. S4, E and F). Both of these (bio)inks showed low yield stresses (crossover of  $G'$  and  $G''$ ) at the (bio)printing temperature range, enabling (bio)ink extrusion at low shear stresses (Fig. 2C).

During the coaxial extrusion process, the flow of  $\text{CaCl}_2$  in the core allowed for in situ physical cross-linking of the alginate component of the (bio)ink, serving to maintain the tubular shape of the conduits (36). In addition, a bath containing  $\text{CaCl}_2/\text{mTG}$  solution was used to further cross-link the (bio)printed tubes. Together with properly set (bio)printing parameters, high-quality dual cross-linked hollow tubes could be obtained. As shown in Fig. 2D, the (bio)printed mono- and dual-layered conduits displayed uniform sizes and smooth surfaces. Coaxial extrusion (bio)printing has several prominent advantages in fabricating vascular conduits. First, the

method would produce structurally relevant tubes with tunable diameters and wall thicknesses for both mono- and dual-layered conduits (Fig. 3D and fig. S5). In addition, this approach enabled the high-throughput fabrication of long, continuous tubes (Fig. 2E). For example, up to 19 m of acellular conduits could be continuously extruded without clogging the nozzle in a single (bio)printing session. Moreover, coaxial (bio)printing enabled efficient conduit production with minimized (bio)ink waste, ideal for cost-effective and large-scale fabrication of conduits. As a demonstration, 1 ml of the MALg1Gel15 (bio)ink could be used to generate as long as 165 cm of a monolayered conduit with 150 to  $180 \mu\text{m}$  of wall thickness, and a 232.9-cm dual-layered conduit with the inner wall thickness of 80 to  $100 \mu\text{m}$  (Fig. 2F).

(Bio)inks with different formulations were adopted to produce small-sized vascular conduits of widely tunable mechanical properties. The mechanical properties of the (bio)printed mono- and dual-layered conduits were studied and compared with mouse vena cava and aorta of similar sizes. Figure 2G shows the stress-strain curves of the monolayered conduits (bio)printed using different (bio)inks containing various MALg contents (0.5 to 2%) and gelatin contents (10 to 20%). Young's modulus and tensile strength of the (bio)printed tubes are very sensitive to content of MALg instead of gelatin (Fig. 2, H to J). For example, for printed DN hydrogels consisting of 15% gelatin, Young's modulus can increase from 65.3 to 472.0 kPa with increasing MALg content from 0.5 to 2%. The (bio)printed DN hydrogel tubes containing an alginate content of 0.5% were mechanically weak, while the stiffness and strength of the (bio)printed tubes with 2% MALg were much higher than those of the mouse vein. In contrast, the DN hydrogel tubes consisting of 1% MALg had mechanical properties matching the native mouse vena cava's tensile modulus, failure strain, and ultimate tensile strength. However, no significant difference in mechanical strength was observed among the 10 to 20% gelatin tubes with fixed alginate. In terms of mechanical properties, the MALg1Gel15 hydrogel-based tubes had the strength of 538.0 kPa and the failure strain of 183.9%, similar to those of mouse vena cava of 738.1 kPa and 134.7%, respectively. Figure 2K and movie S1 show that the MALg1Gel15 tubes and mouse vena cava could be stretched to similar lengths. Therefore, considering both mechanical properties and printability, the MALg1Gel15 (bio)ink was selected as the optimal (bio)ink for the (bio)printing of the conduits. It was noted a significant difference in mechanical properties for the MALg1Gel15 hydrogel films and (bio)printed conduits. Compared with the film samples, the conduits exhibited enhanced stiffness and strength likely due to the shearing-induced alignment of alginate and gelatin chains in the longitude direction during coaxial extrusion (bio)printing (37, 38).

Notably, the DN hydrogel-based tubes also exhibited good physiological mechanical stability. The MALg1Gel15 tubes maintained a stable stiffness in cell culture medium (e.g., SMC medium) for up to 2 weeks evaluated (fig. S6, A and B). The satisfactory physiological stability of the current DN hydrogels could be attributed to the dense ionic cross-linking by the higher guluronate/mannuronate blocks ratio of the used alginate (39).

We also (bio)printed dual-layered vascular conduits to mimic the artery with two different layers. The mechanically robust MALg1Gel15 hydrogel was used as the inner layer to provide mechanical support, while the weaker hydrogel (bio)inks containing 3% GelMA and different types and concentrations of alginates were used for bioprinting the outer layer to support cell growth. When using MALg from 1 to

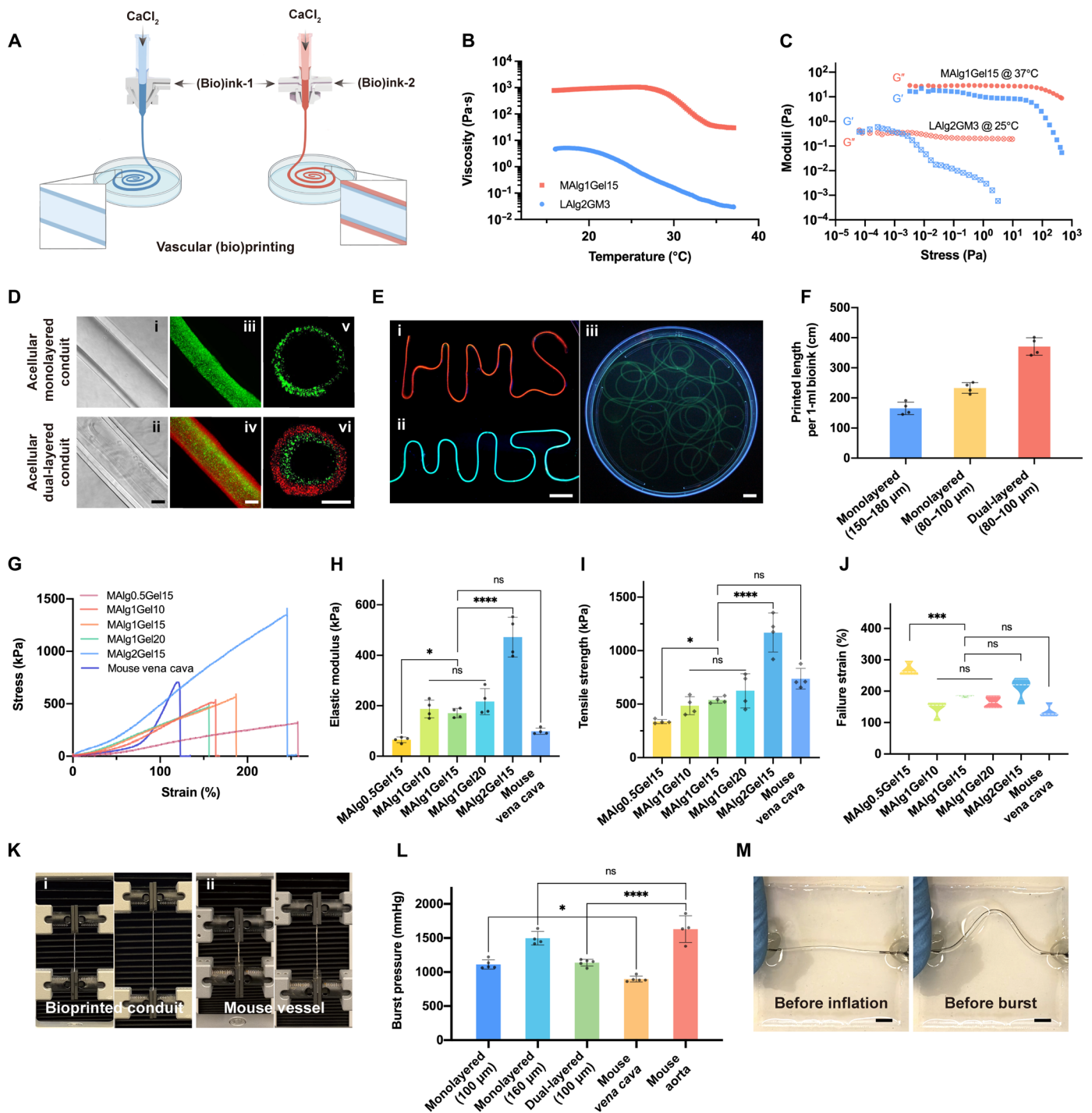


**Fig. 2. Microfluidic extrusion (bio)printing and mechanical properties of tubular conduits.** (A) Schematics of microfluidic extrusion (bio)printing of monolayered and dual-layered vascular conduits. (B) Temperature-dependent viscosities of the alginate-gelatin and the alginate-GelMA hybrid (bio)inks. (C) Shear storage moduli (blue) and loss moduli (red) as a function of shear stress on the alginate-gelatin and the alginate-GelMA hybrid (bio)inks. (D) Representative lateral-view bright-field images (i and ii) and fluorescence microscopic images (iii and iv), as well as cross-sectional-view fluorescence microscopic images (v and vi) of monolayered (top) and dual-layered (bottom) hollow tubes. Scale bars, 200  $\mu\text{m}$ . (E) Fluorescence microscopic images of (bio)printed hollow conduits (i, an "HMS"-shaped tube; ii, a "MIT"-shaped tube; iii, a randomly placed long tube). Scale bars, 1 cm. (F) Quantitative evaluations of high-throughput (bio)printing of tubes using 1 ml of (bio)inks. Comparisons of mechanical properties of (bio)printed vascular tubes using different (bio)inks and mouse vena cava: tensile stress-strain curves (G), tensile strengths (H), Young's moduli (I), and failure strains (J). \* $P < 0.05$ , \*\*\* $P < 0.001$ , and \*\*\*\* $P < 0.0001$ . (K) Photographs of tensile tests for (bio)printed monolayered tubes and mouse vena cava. (L) Comparisons of burst pressures for (bio)printed tubes with different sizes and compositions and native vessels. \* $P < 0.05$  and \*\*\*\* $P < 0.0001$ . (M) Photographs of (bio)printed monolayered tubes before and after inflation during burst pressure test. Scale bars, 1 cm.

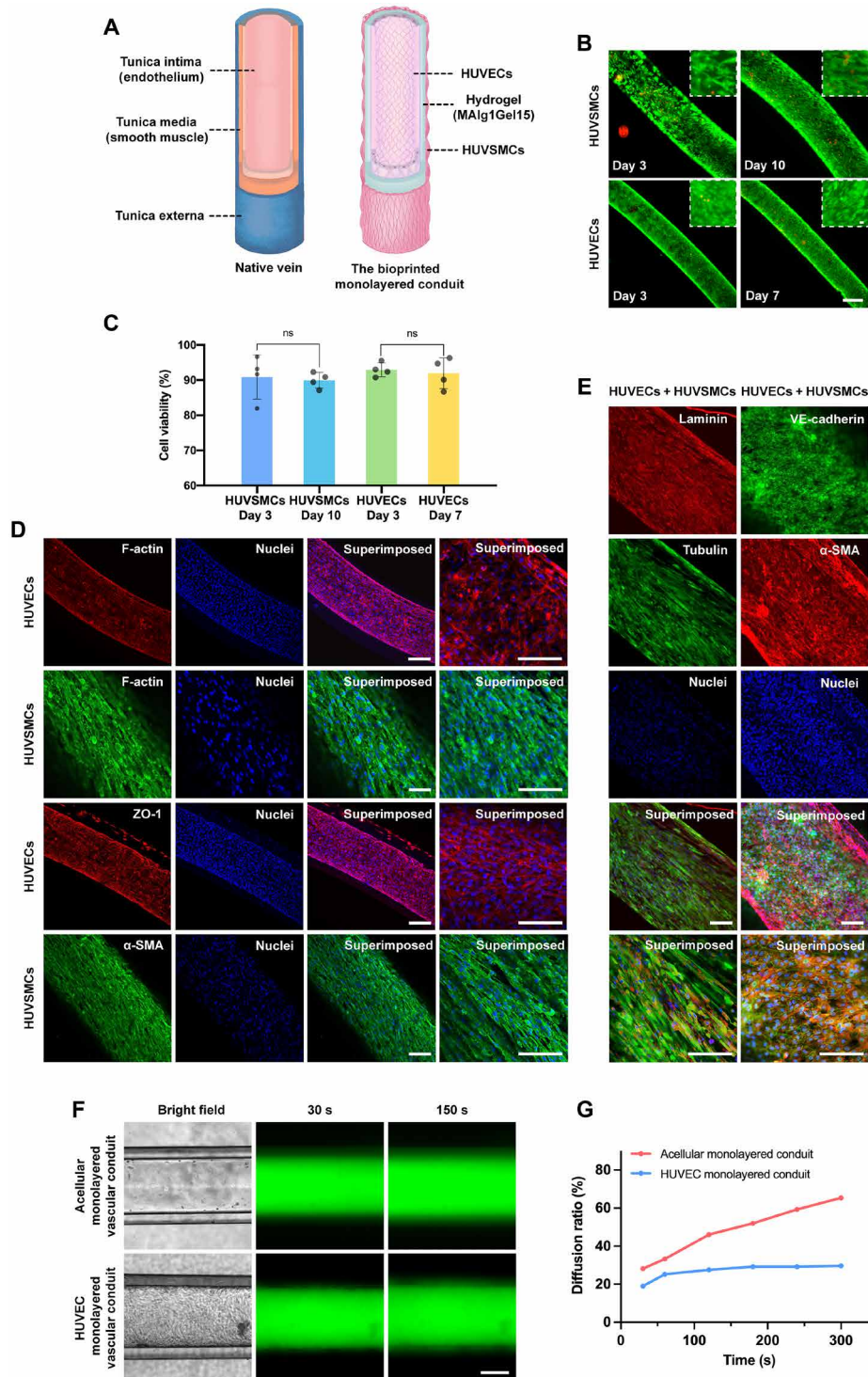


**Fig. 3. Structural and biological functions of (bio)printed venous conduits.** (A) Schematics showing structures of the native vein and 3D (bio)printed venous conduit. (B) Fluorescence microscopic images showing the viability of HUVMSCs and HUVECs at different time points of culture. Green, live cells; red, dead cells. Scale bar, 200  $\mu$ m. (C) Quantified viability of HUVMSCs and HUVECs at indicated time points. (D) Fluorescence confocal images of the immunostained venous conduits exhibiting expressions of F-actin by both HUVMSCs and HUVECs, ZO-1 by HUVECs, and  $\alpha$ -SMA by HUVMSCs for cell separately cultured. The cells were counterstained with 4',6-diamidino-2-phenylindole (DAPI) for nuclei. Scale bars, 100  $\mu$ m. (E) Fluorescence confocal images of the immunostained venous conduits exhibiting expressions of laminin and VE-cadherin by HUVECs, and Tubulin and  $\alpha$ -SMA by HUVMSCs for cell cocultured. The cells were counterstained with DAPI for nuclei. Scale bars, 100  $\mu$ m. (F) Diffusion of 3- to 5-kDa FITC-Dex in (bio)printed monolayered conduits in the absence (top) and presence (bottom) of endothelium formed by HUVECs in the lumens. Scale bar, 200  $\mu$ m. (G) Quantified 3- to 5-kDa FITC-Dex diffusion ratio changes in the absence and presence of endothelium formed by HUVECs in the lumens of monolayered conduits.

0.5%, Young's modulus of the dual-layered tubes decreased from 208.5 to 110.2 kPa (fig. S7). To further reduce the tube's stiffness, LAlg2GM3 were formulated as the (bio)ink (LAlg2GM3) to (bio) print the outer layer of the dual-layered conduits. The resultant tubes had a low Young's modulus of 63.4 kPa while retaining a high stretchability (240.4%), falling in the similar range of the mouse aorta (58.9 kPa and 158.1%, respectively; fig. S7).

Besides, we measured the burst pressures of the (bio)printed mono- and dual-layered conduits to illustrate their similarities to native vessels. According to the Laplace's law, burst pressure is positively correlated with the wall thickness (40). The mouse vena cava and aorta with similar dimensions to the (bio)printed tubes were used as benchmarks. These vascular conduits were highly inflatable and could be tied by 5-0 sutures to the metal connectors (fig. S8 and movie S2). The monolayered conduits (100  $\mu\text{m}$  in wall thickness) exhibited a slightly higher burst pressure (1113.1 mmHg) than that of the mouse vena cava (897.1 mmHg) with a similar wall thickness (Fig. 2L). The burst pressure increased to 1497.6 mmHg at a wall thickness of 160  $\mu\text{m}$ . The 100- $\mu\text{m}$  wall thickness of the dual-layered conduits had a burst pressure of 1137.8 mmHg, which was slightly lower than that of the mouse aorta (1630.9 mmHg). The above results suggested that the (bio)printed DN hydrogel conduits using our optimized (bio)inks were structurally and mechanically relevant to the native vessels to a reasonable extent.

### Perfusability and permeability of (bio)printed conduits

Perfusability and selective permeability, the basic functions of blood vessels, allow the flow and diffusion of small molecules through the wall while retarding or blocking the transport of macromolecules (41). In most of the previously reported studies, including those reported by us (26, 27), (bio)printed hydrogel-based vascular conduits are vulnerable and mechanically weak. These vascular conduits would oftentimes fail to withstand physiological pressure exerted by the flow, limiting their *in vitro* and *in vivo* applications. This fact has been deemed as a common drawback for many of these coaxially extruded hollow conduits (29, 42).

Nevertheless, the (bio)printed tubes developed in this study were tough enough to withstand surgical knots and amenable to insertion and fixation of blunt metal needles, which are important for postbioprinting studies and applications. To assess perfusability and permeability, these (bio)printed tubes were connected to metallic connectors in a bioreactor and maintained a closed circulation system using a peristaltic pump (fig. S8). The fluorescein isothiocyanate (FITC)-conjugated dextran (FITC-Dex) of two different molecular sizes, 3 to 5 and 150 kDa, representative of small molecules and macromolecules, respectively, was then perfused through the (bio)printed tubes. FITC-Dex (150 kDa) could barely diffuse through the wall of the monolayered conduit during the 24-hour perfusion period, whereas the 3- to 5-kDa FITC-Dex rapidly penetrated in a short time and was further distributed throughout the bioreactor reservoir in the following hours as indicated by the remarkable differences in fluorescence intensities in the reservoir (fig. S9, A to D). Similar diffusion profiles were observed in the dual-layered conduits for both 3- to 5-kDa FITC-Dex and 150-kDa FITC-Dex (fig. S9, E to H). A 16-fold reduction was measured in the permeability of 150-kDa FITC-Dex as compared to that of 3- to 5-kDa FITC-Dex in monolayered conduits, whereas the value for the dual-layered conduits markedly decreased from  $7.2 \times 10^{-3}$  to  $0.6 \times 10^{-3} \text{ cm s}^{-1}$  (fig. S10). These results suggested the selective

permeability of molecules across the walls of the (bio)printed conduits. We were able to maintain the perfusion of FITC-Dex (150 kDa) or medium through the vascular conduits for up to 3 days tested without any leakage (movie S4), demonstrating their potential for long-term applications under physiological circulation conditions. An ideal vascular conduit should support the flow of blood and withstand the pressures exerted by the blood flow immediately upon implantation *in vivo* (43). Therefore, we further assessed the perfusion of red blood cells (RBCs) through a long monolayered conduit without noticeable rupture or leakage (movie S3), illustrating that the (bio)printed conduits may have the potential to receive and withstand the pressures exerted by the blood flow while maintaining structural integrity.

### Generation of venous conduits

The venous blood vessel wall consists of the inner endothelium composed of ECs, the middle muscular layer composed of SMCs and elastic tissue, and an outer fibrous connective tissue layer (44). Veins and venules have thinner muscular walls than arteries and arterioles, largely because the pressures and rates of blood flow in veins and venules are much lower (Fig. 3A) (44). To recreate the native vein-like venous conduit with functional endothelial and muscular layers, HUVSMCs were first seeded on the outer surface of the (bio)printed monolayered conduit. After 3 days of culture under static conditions at 37°C, a compact layer of HUVSMCs was formed across the entire outer surface of the conduit. HUVECs were then perfused and allowed to attach in the inner lumen of the same conduit already having the outer smooth muscle layer. After incubation of the conduit under similar culture conditions for additional 7 days (thus a total of 10-day culture), a hollow venous conduit with a layer of confluent endothelium in the lumen and a thin, smooth muscle sheath on the outer surface was eventually constructed for further characterizations. Here, to increase the cell-seeding efficiency, we created a hydrophobic cell-seeding mold made of the mixture of polydimethylsiloxane (PDMS) and wax with grooves present, whose sizes matched the printed conduits. The seeded cells in the confined grooves selectively attached on hydrophilic surfaces of the hydrogel conduits placed within, rather than the hydrophobic surface of the mold. The viabilities of postseeded HUVSMCs were assessed at days 3 and 10, while those of postseeded HUVECs were assessed at days 3 and 7 of HUVEC seeding (i.e., days 6 and 10 of HUASMC seeding on the same conduit). As shown in Fig. 3 (B and C), the viability values of HUVSMCs were 90.9% at day 3 and 89.9% at day 10, while those of HUVECs were 92.9% at day 3 and 92.0% at day 7, respectively.

The proliferation and morphologies of both HUVECs and HUVSMCs in the (bio)printed and cellularized venous conduits were assessed by F-actin staining. The expression of tight junction proteins, zonula occludens-1 (ZO-1), by HUVECs indicated the formation of intercellular junctions between the cells necessary for the proper functioning of the endothelial layer. Similarly, expression of  $\alpha$ -smooth muscle actin ( $\alpha$ -SMA), an actin isoform that plays a role in contractility of vascular SMCs, by HUVSMCs revealed the successful formation of a muscular layer on the outer surface of the conduit (Fig. 3D). In addition, the expression of laminin by HUVECs indicated that the HUVECs were actively synthesizing laminin, which represents one of the major structural components of the basement membrane and is essential for adhesion of ECs to the basement membrane and shear stress response of blood vessels. Besides  $\alpha$ -SMA, HUVSMCs

were also found to express tubulin, another marker protein of the contractile phenotype of vascular SMCs (Fig. 3E). Expression of these markers by HUVECs and HUASMCs confirmed the successful formation of venous conduits with functional endothelium covering the inner wall of the lumen and a muscular layer across the outer surface.

Endothelium plays a pivotal role as a vascular barrier in controlling the extravasation of biomolecules, nutrients, and cells. This barrier function is proven to be regulated by ECs lining the luminal surfaces of the vessels but not disturbed by SMCs in homeostasis (23). To further evaluate the barrier function of the venous conduits, we assessed the permeability of FITC-Dex (3 to 5 kDa) using the endothelialized venous conduits. The acellular conduits of the same size were used as the control. FITC-Dex was perfused through acellular conduits and endothelialized conduits, separately. Diffusion ratio, which was measured as the ratio of the grayscale area of diffused FITC-Dex in a fixed microscope field at a selected time point, reflected the permeating speed through the conduit. As shown in Fig. 3 (G to H), fig. S11, and movie S5A, FITC-Dex rapidly permeated into the walls of the acellular conduits and then penetrated out from the lumens. In contrast, the presence of the HUVEC layer effectively delayed the diffusion speed of the molecule (movie S5B). Accordingly, these results confirmed the barrier function of the endothelialized 3D (bio)printed venous conduits.

### Generation of arterial conduits

Arteries and arterioles have relatively thick muscular walls (Fig. 4A) because they have to withstand higher blood pressures. Therefore, the arterial conduits with thicker muscular walls were generated by bioprinting of dual-layered vascular conduits composed of the outer HUASMC-encapsulated layer and inner hydrogel layer. HUAECs were subsequently seeded in the lumen of the inner wall after the maturation of the HUASMCs. While the same ink formulation as used for (bio)printing the venous conduits (MAlg1Gel15) was used for generating the inner robust hydrogel layer, the cell-friendly outer-layer bioink was optimized to enable desirable cellular behaviors. The initial elastic modulus of a hydrogel has a notable impact on the morphology and proliferation of cells embedded in it. In general, materials with lower stiffness values and larger mesh sizes are beneficial for cell spreading and proliferation (45). Accordingly, the mechanical properties of the (bio)printed monolayered hollow tubes using various (bio)ink formulations consisting of different combinations of alginate and gelatin or GelMA were first tested. For a fixed GelMA content of 3% (GM3), the initial stiffness of the tubes was influenced by both alginate content and type. As shown in fig. S12 (A to C), the initial Young's moduli of the samples containing 2% LAlg were below 100 kPa. In comparison, the MAlg1GM3 tubes produced with MAlg had a much higher Young's modulus (265.3 kPa).

We further assessed the changes in their physiological stability in SMC culture medium. In fig. S12 (D and E), the modulus of the LAlg2Gel3 tubes markedly dropped from 62.0 to 29.6 kPa after 4 hours of incubation in the SMC medium. Because the physical network LAlg can be rapidly degraded via ionic exchange by the medium. The stable plateau modulus for extended treatment time was attributed to the chemically cross-linked network of gelatin. The high stiffness of LAlg2Gel3 would restrict proper cellular activities. To this end, we changed the gelatin component to GelMA with fewer lysine residues so as to reduce the enzymatic cross-linking.

Although the resulting LAlg2GM3 tubes had a high initial stiffness of 112.3 kPa due to dense ionic cross-linking, after medium treatment, the mechanical properties of the LAlg2GM3 tubes became too soft to perform tests after 1-day culture in SMC medium. The above results suggest that LAlg-based hydrogels have poor physiological stability in a buffer solution or medium. Consequently, the LAlg2GM3 hydrogel exhibited prominent stiffness reduction during culture, which is beneficial for cellular functions. In contrast, the inner-layer material of MAlg1Gel15 as mechanical support of the tubes showed good physiological stability (fig. S6), suggesting that the type of alginate plays a key role in determining the stability of the resulting hydrogels.

The cellular behaviors in the above bioinks were further assessed. Bioinks composed of 3% GelMA and 0.5, 1, or 2% LAlg enabled spreading of HUASMCs, as indicated by F-actin staining results (fig. S13). By contrast, the bioinks containing MAlg inhibited the growth of HUASMCs even at alginate content as low as 0.5%. It was also noted that the bioinks containing LAlg at less than 2% exhibited poor printability. Accordingly, LAlg2GM3 was selected as the optimal bioink with good cellular behaviors and printability for bioprinting the outer layers of the conduits with HUASMCs encapsulated. The bioprinted HUASMC-laden conduits were incubated at 37°C for at least 14 days until a tight volume of HUASMCs was formed within the outer layers. Figure 4B represents the viability of the bioprinted HUASMCs at days 3 and 10 of bioprinting. F-actin staining of the bioprinted HUASMCs demonstrated the evenly spreading HUASMCs in the arterial conduits (Fig. 4C).

After approximately 14 days, HUAECs were further seeded in the lumen by perfusing the cell suspension, following the similar procedure as used for seeding the venous conduits. After additional 7 days of culture, hollow arterial conduits were obtained with a layer of endothelium layer in the lumen and a relatively thick smooth muscle sheath on the outer surface. The average thickness of the HUASMC layers in the arterial conduits was found to be 55  $\mu\text{m}$ , which was noticeably thicker than that in the venous conduits ( $\sim 20 \mu\text{m}$ ). The expressions of ZO-1 by HUAECs and  $\alpha$ -SMA by HUASMCs revealed the formation of endothelial layer in the lumen wall and compact smooth muscle layer on the outer surface of the conduit (Fig. 4D). Similarly, the barrier function of arterial conduits was also confirmed by perfusing FITC-Dex (3 to 5 kDa). The permeability of FITC-Dex through the endothelialized arterial conduits suggested that the presence of the compact HUAEC layer obviously decelerated the transport rate of these fluorescence molecules when compared to the control without the endothelium (Fig. 4E, figs. S14 and S15, and movie S5, C and D).

Blood vessels, particularly the arteries and arterioles, constantly receive a variety of vasoconstrictor and vasodilator stimuli wherein SMCs in the muscular layer respond to these stimuli causing constriction or dilation to regulate the vascular tone and, hence, blood flow and blood pressure (46). Vasoconstriction is narrowing of lumen as a result of contraction of the SMC layer, whereas vasodilation is widening of lumen resulting from relaxation of SMCs (47). To evaluate the contractility and thus phenotype of HUASMCs in the muscle layer of our bioprinted arterial conduits, phenylephrine, one of the potent vasoconstrictors (48), was applied to the arterial conduits. Because phenylephrine induces vasoconstriction through  $\alpha$ -adrenergic receptor, before contractility evaluations, we assessed the expressions of  $\alpha$ -1a-adrenergic receptor by arterial SMCs in arterial conduits (Fig. 4F).  $\alpha$ -1a-Adrenoceptor stimulation with phenylephrine (10  $\mu\text{M}$ ) elicited a notable reduction of the diameter of the

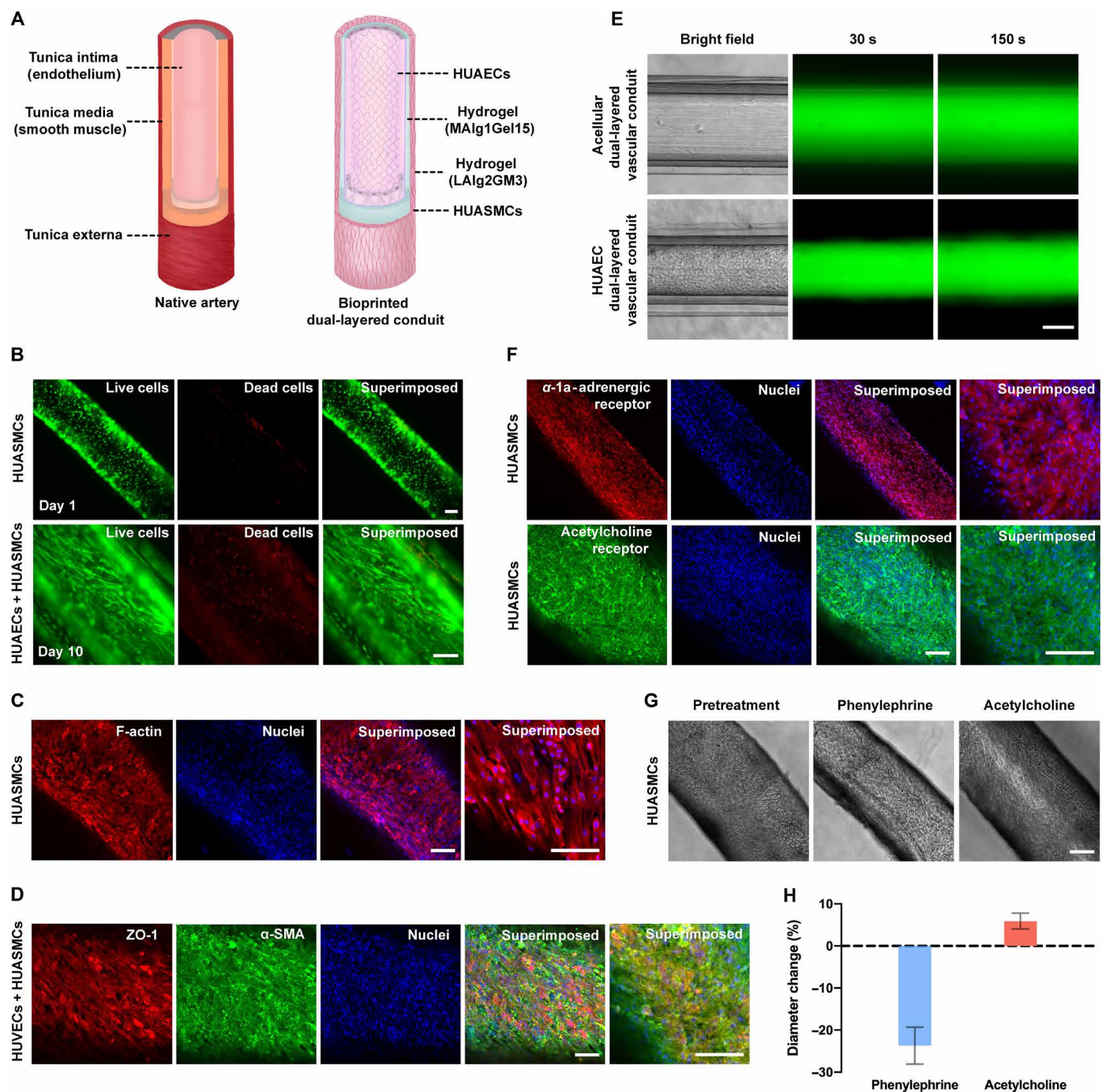


**Fig. 4. Structural and biological functions of (bio)printed arterial conduits.** (A) Schematics showing structures of the native artery and (bio)printed arterial conduit. (B) Fluorescence microscopic images showing the viability of (bio)printed HUASMCs at different time points of culture. Green, live cells; red, dead cells. Scale bars, 100  $\mu\text{m}$ . (C) Fluorescence confocal images of the immunostained artery exhibiting expressions of F-actin by HUASMCs. The cells were counterstained with DAPI for nuclei. Red, F-actin; blue, nuclei. Scale bars, 100  $\mu\text{m}$ . (D) Fluorescence confocal images of the immunostained artery exhibiting expressions of ZO-1 by HUAEs and  $\alpha$ -SMA by HUASMCs. The cells were counterstained with DAPI for nuclei. Red, ZO-1; green,  $\alpha$ -SMA; blue, nuclei. Scale bars, 100  $\mu\text{m}$ . (E) Diffusion of 3- to 5-kDa FITC-Dex in the (bio)printed dual-layered conduits in the absence (top) and presence (bottom) of endothelium formed by HUAEs in the lumens. Scale bar, 200  $\mu\text{m}$ . (F) Fluorescence confocal images of the immunostained artery exhibiting expressions of  $\alpha$ -1a-adrenergic receptor and muscarinic acetylcholine receptor by HUASMCs. The cells were counterstained with DAPI for nuclei. Red,  $\alpha$ -1a-adrenergic receptor; green, muscarinic acetylcholine receptor; blue, nuclei. Scale bars, 100  $\mu\text{m}$ . (G) Vasoactivities of bioprinted arterial conduits in response to phenylephrine and acetylcholine. Scale bar, 200  $\mu\text{m}$ . (H) Quantified changes in diameter of bioprinted arterial conduits in response to phenylephrine and acetylcholine.

arterial conduits, reflecting the constriction of arterial SMCs within the muscle layer of arterial conduits (Fig. 4, G and H). Similarly, studies have shown that acetylcholine, a vasodilator, would relax contractions of vascular smooth muscle induced by phenylephrine, mediated by the M<sub>3</sub> muscarinic acetylcholine receptor (49). As shown in Fig. 4F, arterial SMCs in arterial conduits exhibited the expressions of M<sub>3</sub> muscarinic acetylcholine receptor. The responses to acetylcholine (10 μM) were then examined in precontracted arterial conduits induced by phenylephrine. The application of acetylcholine indeed relaxed phenylephrine-induced contractions of arterial SMCs leading to the dilation of the arterial conduits approximately to the original size (Fig. 4, G and H). Thus, the bioprinted arterial SMCs within the arterial conduits displayed important physiological functions, i.e., vasoconstriction and vasodilation, in response to stimuli by vasoconstrictor and vasodilator.

### In vitro, ex vivo, and in vivo applicability of (bio)printed vascular conduits

The coronavirus disease 2019 (COVID-19) pandemic caused by the infection with SARS-CoV-2 has remarkably affected our lives since December 2019 (50). SARS-CoV-2 binds to the angiotensin-converting enzyme 2 (ACE2) receptor, via spike glycoprotein, for entering the host cells (51). SARS-CoV-2 had infected more than 539 million people, causing more than 6.3 million deaths across the globe (50). New SARS-CoV-2 variants have been continuously evolving because of mutations in the SARS-CoV-2 genome, some of which are classified as variants of concern as they are more aggressive, highly transmissible, vaccine-resistant, and cause more-severe disease manifestations as compared to the original SARS-CoV-2 strain (52). In addition, multiple reinfections and relapses with SARS-CoV-2 have been recorded (53). Notably, although COVID-19 is primarily considered a respiratory disease, it can affect several other vital organ systems, including cardiovascular, renal, and brain systems. For example, recently, clinical observations and in vivo animal studies suggested that the adverse effects of COVID-19 on multiple organs are due to increased vascular dysfunction such as leaky vascular barrier and enhanced expression of von Willebrand factor that caused increased coagulation, cytokine release, and inflammation (54–56).

3D (bio)printed blood vessels that recapitulate key features of native blood vessels can be used as reliable preclinical in vitro models to study the direct vascular responses to the SARS-CoV-2 infections. We thus assessed the applicability of (bio)printed conduits as 3D vascular models for examining SARS-CoV-2 infection using pCoV-VPs and treatment efficacies of antiviral drugs using two clinically approved antiviral drugs, remdesivir (RMD) and amodiaquine (ADQ), which have been given to patients with COVID-19 (57, 58). Blood vessels are prone to SARS-CoV-2 infections because the ACE2 receptor is expressed by all vascular structural cells, including ECs, SMCs, fibroblasts, and pericytes, among other cell types (59, 60).

Before pCoV-VP infection, the expression of ACE2 receptor was assessed for the venous conduits. As shown in Fig. 5A, HUVMSCs within the venous conduits exhibited a high level of expression of the ACE2 receptor. The venous conduits were inoculated with mCherry-labeled pCoV-VPs at the multiplicity of infection of 0.5 for 48 hours to identify the virus susceptibility in vitro in the presence of antiviral drugs. The conduits infected with pCoV-VPs in the absence of drugs were used as the control. After 48 hours of exposure, the infection of cells with pCoV-VPs could be observed under fluorescence microscopy (Fig. 5B). The number of pCoV-VPs in the

infected venous conduits was quantified by measuring luciferase activity. The viral entry in untreated venous conduits was set as 100%. The infection of venous conduits with pCoV-VPs was observed to be reduced to 38.3% in the presence of RMD and 73.2% in the presence of ADQ (fig. S16). Similarly, the cytopathic effect of pCoV-VPs was analyzed by live/dead assay (Fig. 5C) and (3-(4,5-dimethylthiazol-2-yl)-5-(3-carboxymethoxyphenyl)-2-(4-sulfophenyl)-2H-tetrazolium (MTS) assay (Fig. 5D). The cytopathic effects of pCoV-VPs were decreased in the presence of the antiviral drugs while improving the cell viability values and metabolic activities. Thus, these therapeutics notably inhibited the viral entry- and infection-induced cell death by the pCoV-VPs expressing the SARS-CoV-2 spike proteins.

Last, to explore the future translational potential as vascular grafts, the (bio)printed conduits of different diameters were connected to native vessels. We initially (bio)printed a tube with a diameter of 1 mm and glued it to an ex vivo explanted mouse aorta to achieve anastomosis. Orange fluorescent beads were perfused from one open end of the (bio)printed conduit to pass the joining point and exit from the open end of the mouse aorta. As demonstrated in Fig. 5E (i and ii) and movie S6, the dye went through the entire leak-free lumen smoothly. To enhance this concept, we subsequently used a freshly isolated popliteal vein harvested from a human patient receiving bypass surgery to connect with a (bio)printed larger conduit (5 mm in diameter). Similarly, no leakage was observed during the perfusion of green fluorescence beads from the natural vein to the (bio)printed vascular conduit (Fig. 5E, iii and iv, and movie S7). To this end, we conducted a proof-of-concept test in vivo in mice (Fig. 5F, i), where the vena cava was exposed (Fig. 5F, ii), followed by gluing a sterile (bio)printed vascular conduit to it from both ends. After the release of the clamps, the bloodstream was observed to flow through the vena cava to the (bio)printed conduit and to vena cava quickly without noticeable leakage (Fig. 5F, iii). This set of results illustrated that the (bio)printed conduits could be anastomosed to native vessels in various scenarios, direct evidence for potential in vivo vascular reconstruction applications, although the need for further optimization is acknowledged.

In summary, we developed DN tough hydrogel (bio)inks consisting of gelatin (or GelMA) and alginate with suitable rheological properties and cell-benign cross-linking for microfluidic (bio)printing of engineered small-diameter vascular conduits. The bioprinted venous and arterial conduits, consisting of the inner endothelial layer and outer smooth muscle layer, mimicked important features of the native veins and arteries, respectively. They exhibited superior mechanical properties, including burst pressure, elasticity, stretchability, and stiffness, comparable to those of the native vessels. In addition to the perfusability and selective permeability, expressions of relevant biomarkers were observed in the bioprinted conduits. Critically, the compact endothelial monolayer provided barrier function, and the thicker smooth muscle layer of arterial conduits allowed the conduits to constrict and dilate similar to native arterioles. The (bio)printed vascular conduits could also serve as good in vitro vascular models to study vascular responses to viral infection and the efficacies of antiviral drugs. In addition, these (bio)printed conduits revealed the potential to be used as vascular grafts for in vivo applications. Compared to the existing progress in the field, the coaxially (bio)printed vascular conduits in this study has advantages in items of both physical properties and physiological stability (table S1). However, our technology is not without

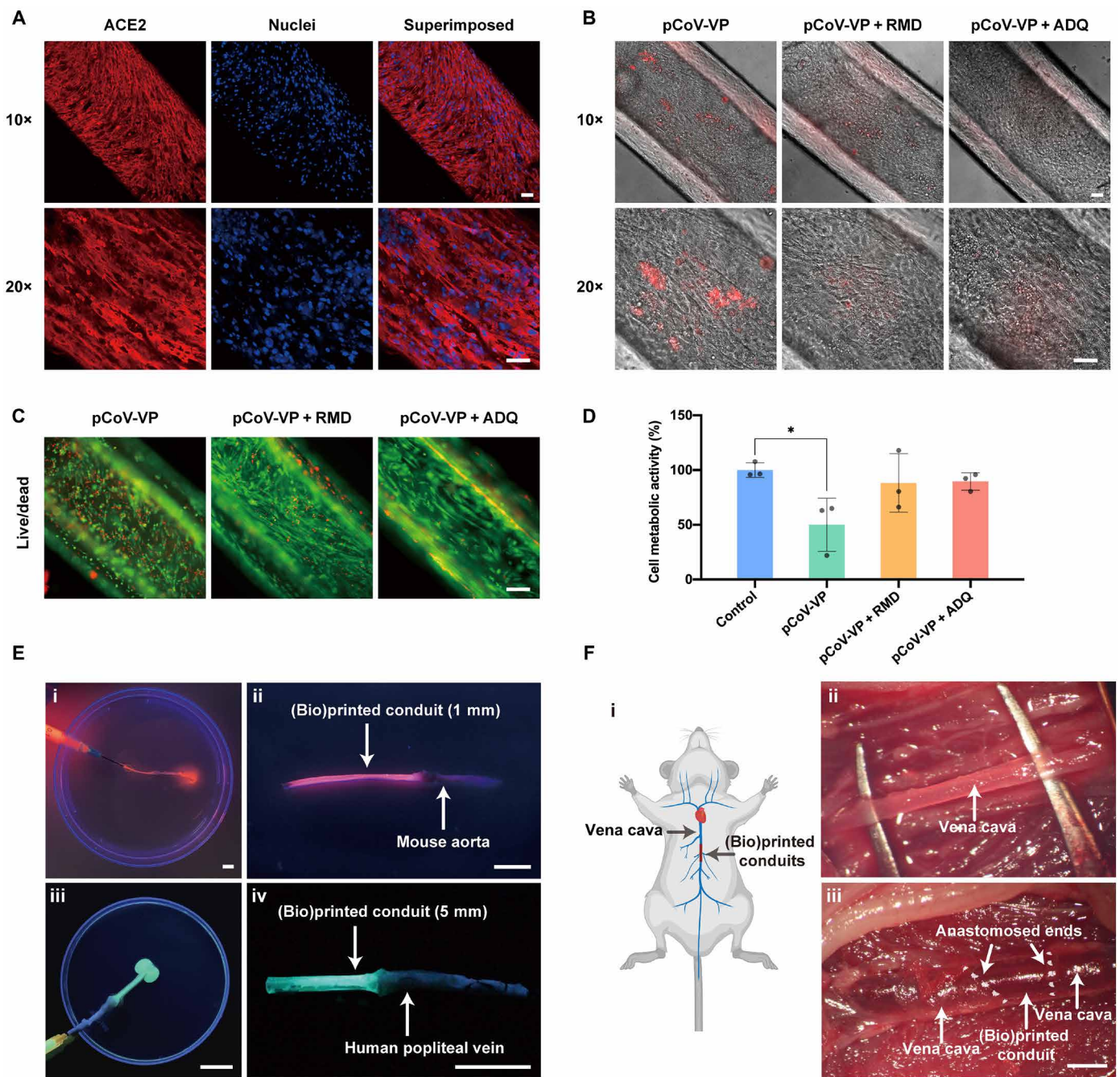


**Fig. 5. In vitro, ex vivo, and in vivo applications of (bio)printed vascular conduits.** (A) Fluorescence confocal images showing the expression of ACE2 receptors by HUVMSCs and HUVECs in the bioprinted vascular conduits. The cells were counterstained with DAPI for nuclei. Red, ACE2 receptors; blue, nuclei. Scale bars, 100  $\mu$ m. (B) Fluorescence and bright-field microscopic images showing mCherry-expressing pCoV-VP-infected HUVMSCs and HUVECs in the bioprinted vascular conduits in the absence of antiviral drug (pCoV-VPs) and in the presence of 10  $\mu$ M of RMD (pCoV-VPs + RMD) or 10  $\mu$ M ADQ (pCoV-VPs + ADQ). Scale bars, 100  $\mu$ m. (C) Fluorescence microscopic images showing live/dead staining of cells in the bioprinted vascular conduits after pCoV-VP infection without antiviral drugs (pCoV-VPs) and with 10  $\mu$ M of RMD (pCoV-VPs + RMD) or 10  $\mu$ M of ADQ (pCoV-VPs + ADQ). Green, live cells; red, dead cells. Scale bar, 100  $\mu$ m. (D) MTS assay showing metabolic activities of cells in the bioprinted vascular conduits after pCoV-VP infection in the absence and presence of antiviral drugs. \* $P < 0.05$ . (E) Ex vivo connection and perfusion of bioprinted vascular conduits linked to native vessels by biogluce. (i and ii) A small-sized printed vascular conduit (1-mm outer diameter) anastomosed with a mouse aorta; (iii and iv) a printed larger-sized (5-mm outer diameter) vascular conduit anastomosed with a human popliteal vein. Scale bars, 20 mm. (F) In vivo implant and perfusion between mouse vena cava and a printed vascular conduit in mouse. (i) Schematic diagram showing in vivo connection between mouse vena cava and a (bio)printed vascular conduit; (ii) exposure of mouse vena cava; (iii) perfusion of the blood after anastomosis. Scale bar, 1 mm.

limitations. For example, despite enhanced high toughness, suturing these hydrogels tubes was found not easy because of their insufficient suture-retention abilities. Additional efforts are being devised to further improve our (bio)ink formulations. In some regions of the conduits, the SMCs on the conduits oriented longitudinally in parallel with the conduits, which is different from the orientation of SMCs in the native vessels despite the level of functions observed. In this regard, circumferential alignment of SMCs may be more desired for engineered blood vessels to mimic their native structures and functions. Further studies could focus on achieving circumferentially aligned SMCs on these (bio)printed vascular conduits. Moreover, comprehensive in vivo evaluations remain to be conducted.

## MATERIALS AND METHODS

### Materials

This study did not generate new unique reagents. Gelatin from porcine skin (type-A, 300 bloom, with an isoelectric point of 7.0 to 9.5), methacrylic anhydride, sodium alginate (71238, medium viscosity), sodium alginate (A1112, low viscosity), FITC-Dex (3 to 5 and 150 kDa), phenylephrine, acetylcholine, CaCl<sub>2</sub>, bovine serum albumin (BSA), Triton X-100, and EDTA were obtained from Sigma-Aldrich (Burlington, MA, USA). Paraformaldehyde (16%) was purchased from Electron Microscopy Sciences (Hatfield, PA, USA). mTG was purchased from Ajinomoto North America Inc. (Fort Lee, NJ, USA). Fetal bovine serum (FBS), Dulbecco's phosphate-buffered saline (DPBS), Dulbecco's modified Eagle's medium, trypsin-EDTA, 2-[4-(2-hydroxyethyl) piperazin-1-yl]-ethane sulfonic acid [Hepes buffer, 25 mM (pH 7.4)], and antibiotic-antimycotic solution stabilized (anti-anti; 100×) were from Life Technologies (Carlsbad, CA, USA). 4',6-diamidino-2-phenylindole (DAPI), Live/Dead Viability/Cytotoxicity Kit, Alexa Fluor 594-phalloidin, Alexa Fluor 488-phalloidin, dialysis membrane [molecular weight ( $M_w$ ) cutoff: 12,000 to 14,000 Da], and rabbit  $\alpha$ -1a-adrenergic receptor antibodies were obtained from Thermo Fisher Scientific (Cambridge, MA, USA). Endothelial growth medium (EGM-2) and endothelial growth supplements were obtained from Lonza (Walkersville, MD, USA), and the SMC growth medium-2 (SmGM-2) along with growth supplements was obtained from PromoCell (Heidelberg, Germany). Rabbit anti-ZO-1 antibody, rabbit anti-vascular endothelial (VE)-cadherin antibody, mouse anti- $\alpha$ -SMA antibody, rabbit muscarinic acetylcholine receptor antibody, and Alexa Fluor 594- or 488-conjugated goat anti-rabbit or goat anti-mouse secondary antibodies were purchased from Abcam (Cambridge, MA, USA). Rabbit ACE2 antibody was purchased from Rockland (Limerick, PA, USA). RBCs collected in citrate, phosphate, dextrose, adenine formula 1 were purchased from Research Blood Components (Watertown, MA, USA). PDMS was purchased from Dow Corning Inc. (Midland, MI, USA). All other chemicals used in this study were obtained from Sigma-Aldrich (Burlington, MA, USA) unless otherwise mentioned.

### Animal and human tissue collection

All animal-relevant experiments were conducted in accordance with protocols approved by the local Institutional Animal Care and Use Committee and complied with the Guide for the Care and Use of Laboratory Animals. Nine-week-old male C57BL/6J mice weighing 20 to 24 g were purchased from the Jackson Laboratory (Bar Harbor, ME). The animals were maintained on a 12-hour light/dark cycle, and they received water and standard chow ad libitum.

Discarded human vascular tissues were harvested under a local institutional review board-approved protocol. The sample was stored at  $-80^{\circ}\text{C}$  until use.

### Synthesis of GelMA

GelMA was synthesized following the previously described protocol we introduced (61–63). Briefly, 10.0 g of type-A gelatin from the porcine skin was added into 100 ml of DPBS and dissolved at  $50^{\circ}\text{C}$  under a magnetic stirrer for 30 min. Then, 5.0 ml of methacrylic anhydride was added dropwise to the gelatin solution and kept stirring at  $50^{\circ}\text{C}$  for 3 hours. The reaction was quenched by 100 ml of warm DPBS ( $40^{\circ}\text{C}$ ). Next, the reaction product was dialyzed against distilled water at  $40^{\circ}\text{C}$  for 5 days using a dialysis membrane ( $M_w$  cutoff: 12,000 to 14,000 Da). Last, the solution was filtered by a 0.2- $\mu\text{m}$  filter and lyophilized to yield a white porous foam, which was stored at  $-20^{\circ}\text{C}$  for further use.

### Hydrogel film fabrication

The biopolymers were all dissolved in distilled water to prepare the hydrogel precursors. Pure alginate hydrogel was obtained by ionic cross-linking of 1% alginate solution (pH 7.0) using a 2% CaCl<sub>2</sub> solution. Liquid-form hydrogel precursors of 15% gelatin (pH 5.4) and hybrid (bio)ink containing 1% alginate and 15% gelatin (pH 5.5) were sandwiched between two glasses by 0.3-mm plastic spacers. After cooling down  $4^{\circ}\text{C}$  for 2 to 3 min, the obtained physical gel was transferred to CaCl<sub>2</sub>/mTG solution bath. After curing at room temperature for 30 min, the hydrogel was further cured at  $37^{\circ}\text{C}$  overnight to obtain hydrogel films. To fabricate ionic and covalent single-network hydrogels, the cross-linker bath was switched to 2% CaCl<sub>2</sub> and 2% mTG, respectively. The dual cross-linked hydrogels were also treated by the 3% EDTA to selectively remove the ionic cross-links in the DN hydrogels.

### Rheology tests

Rheology measurement was conducted on a rheometer (DHR-3, TA Instruments, New Castle, DE, USA) using a 1° core plate geometry with a diameter of 40 mm and a gap height of 26  $\mu\text{m}$ . Apparent viscosities and shear stresses as a function of shear rate (0.01 to 200  $\text{s}^{-1}$ ) were measured via steady-state flow sweep at different temperatures. Oscillation temperature sweeps were performed over the range from  $15^{\circ}$  to  $37^{\circ}\text{C}$  with a heating rate of  $2^{\circ}\text{C min}^{-1}$  using an oscillatory frequency of 1 Hz and a shear strain of 1%. Amplitude sweep was measured as a function of shear strain (0.01 to 2000%) via oscillation experiments using a fixed frequency of 1 Hz at constant temperatures.

### Microfluidic extrusion (bio)printing of acellular monolayered and dual-layered conduits

We used two types of coaxial extrusion systems with two or three channels to (bio)print venous and arterial conduits, respectively. To achieve broadly geometry-tunable printability and reassemblability benefiting recycling of the nozzles, we first designed (bio)printing nozzle systems (BNSs) in a computer-aided design software (SolidWorks, Dassault Systèmes, Vélizy-Villacoublay, France). Then, clear resin (green translucent ultraviolet resin, Anycubic, Shenzhen, China) was used to print all the pieces of the BNSs by a commercial stereolithography apparatus printer (Anycubic Photon), which granted great versatility in designs and very fast fabrication times (fig. S3). The nozzles were assembled using commercial screws and bolts and

were put together with silicon tubes using commercial blunt needles. The BNSs could be easily disassembled to wash or switch every piece and worked well as the traditional coaxial extrusion nozzles made entirely from commercial needles (27, 29, 64).

BNSs with two coaxial channels were used to (bio)print monolayered acellular tubular conduits (Fig. 2A) using the (bio)ink composed of medium-viscosity alginate (0.5, 1, and 2%) and gelatin (10, 15, and 20%).  $\text{CaCl}_2$  solution (2%) flowing in the core layer acted as the cross-linker for alginate in the hybrid (bio)ink (Fig. 2A). (Bio)inks containing 2% LAIg and gelatin or GelMA were also used to (bio)print tubes for mechanical measurement and physiological stability study. The (bio)printed tubes were later cross-linked with  $\text{CaCl}_2/\text{mTG}$  overnight, resulting in hollow monolayered acellular conduits with DN hydrogel walls. BNSs with three coaxial channels were used to (bio)print dual-layered acellular tubular conduits.

### Mechanical tests

The tensile and pure-shear tests for film and tube samples were performed on a universal tensile machine (Instron 3342, Norwood, MA, USA) with a load cell capacity of 100 N. Rectangular samples with 0.3 to 0.4 mm in thickness and 6 mm in width were cut from the film samples for mechanical measurements. For the pure-shear test, a precut with a length of 2 mm was introduced in the middle. (Bio)printed tubes with a diameter of 800 to 900  $\mu\text{m}$  and a thickness of 200 to 300  $\mu\text{m}$  were also used for the tensile test. The gauge length for all the samples was set at approximately 8 mm, and the stretching rate was fixed at 0.5  $\text{min}^{-1}$ . In loading-unloading test, the film samples were first loaded to 25% strain and unloaded using the same stretching rate. Successive loading-unloading test was also conducted using increasing applied maximum strains. The nominal stress was defined as the applied force divided by the cross-sectional area in the undeformed state. The strain was defined as the elongated sample length divided by the initial length. The tensile modulus was determined by the slope of the stress-stretch curve within the 3% strain. The toughness and hysteresis ratio of hydrogels was calculated according to literature (65). The fresh native blood vessels, including the mouse vena cava (approximately 800  $\mu\text{m}$  in outer diameter and 110  $\mu\text{m}$  in thickness) and aorta (approximately 1200  $\mu\text{m}$  in diameter and 180  $\mu\text{m}$  in thickness) with similar size to the (bio)printed acellular conduits and were harvested for tensile test.

### Measurement of burst pressures

Hollow tubes of different sizes were fabricated, and the mouse vena cava and aorta were used as controls. The acellular vascular conduits were highly inflatable and able to be tied to metal needles of the bioreactor by surgical knots (5-0 sutures). The two ends of each tube were fixed onto two blunt needles. Then, it was well inflated by pressured air without leakage. To quantify the burst pressure, one end of each sample was closed by suture, while the other end was cannulated to a blunt needle connecting to a gas tank and a pressure sensor. Burst pressure was measured by pressurizing the sample with compressed air until failure and calculated considering zero external pressure and no axial loading.

### Permeability and diffusion tests

To evaluate the perfusability, a narrow but long monolayered tube (800  $\mu\text{m}$  in diameter and 25 cm in length) was (bio)printed and randomly coiled in a vial filled with deionized water, leaving the two ends outside, followed by perfusing RBC suspension from one of the ends.

To evaluate the barrier performances of the (bio)printed conduits, a PDMS mold with one or two culture medium reservoirs was fabricated, and two or four blunt needles matching the investigated tube size were inserted into the two sides of each reservoir, in which the medium was filled (fig. S8). Sequentially, a (bio)printed vascular conduit was fixed between the two needles by surgical knots. Then, the conduit-connected bioreactor further linked to a peristaltic pump (Elemental Scientific, Omaha, NE, USA) that was loaded by 3- to 5- or 150-kDa FITC-Dex. During permeability characterizations, all parameters of the circulation system and the fluorescence microscope settings between groups, including perfusion rate (4  $\text{ml min}^{-1}$ ), fluorescence dye concentration, tube length, tube size, medium volume, exposure time, and brightness threshold, remained unchanged.

To explore the selective permeability for small and large molecules, we chronologically imaged the fluorescence of the tubes at predefined time points of 10 min, 4 hours, 8 hours, and 24 hours and measured the fluorescence intensity profiles across the central portion of the reservoir in these images by the method reported in the literature (66). To quantify the difference, diffusional permeability was calculated according to an equation published (67)

$$P_d = \frac{1}{l_1 - l_b} \left( \frac{l_2 - l_1}{t} \right) \frac{d}{4}$$

where  $P_d$  is the diffusional permeability coefficient,  $l_1$  is the average intensity at the initial time point,  $l_2$  is the average intensity at the given time ( $t$ , approximately 30 min),  $l_b$  is the background intensity (before introducing FITC-Dex), and  $d$  is the channel diameter. The measurements are performed on the (bio)printed conduits with and without endothelium.

To verify the barrier function of the endothelium of the cell-seeded (bio)printed vascular conduits, the fluorescence images and videos were captured in the first 10 min since the onset of perfusion. They were subsequently processed into greyscale images in ImageJ (National Institutes of Health, Bethesda, MD, USA), followed by calculating the fluorescence area ratio of each image, which was defined as the diffusion rate, according to the method published (68).

### Cell culture

Primary HUVSMCs were purchased from ScienCell Research Laboratories (Carlsbad, CA, USA), whereas primary HUVECs were obtained from Lonza (Walkersville, MD, USA). Primary HUASMCs and primary HUAECs were obtained from PromoCell. Both HUVECs and HUAECs were cultured EGM-2 medium supplemented with endothelial growth supplements and 1% (v/v) anti-anti. Similarly, both HUVSMCs and HUASMCs were cultured in SmGM-2 supplemented with growth supplements and 10% (v/v) FBS and 1% (v/v) anti-anti. The cells were incubated at 37°C and 5%  $\text{CO}_2$  in a 95% humidified cell incubator until 70 to 80% confluency. The respective culture medium was changed every third day.

### Cell seeding in the (bio)printed monolayered tubular conduits

The HUVSMCs at 70 to 80% confluence were trypsinized, centrifuged, and resuspended in medium at  $8 \times 10^6$  viable cells  $\text{ml}^{-1}$ . PDMS-wax (95:5%) mold with multiple straight channels was fabricated. Approximately 100  $\mu\text{l}$  of HUVSMC suspension was first loaded into channels, and end-closed monolayered tubes were placed in the channels individually containing the HUVSMC suspension, followed by

pouring additional 100  $\mu\text{l}$  of HUVMC suspension on the top surfaces of tubes in the channels. After 1 day of incubation at 37°C in the incubator, HUVMCs were found to be selectively attached to the outer surfaces of the tubes rather than the mold surfaces due to the pronounced hydrophobicity of the latter. On day 3 of HUVMC seeding, HUVECs were seeded in the lumen by perfusing 100 to 150  $\mu\text{l}$  of HUVEC suspension at  $1 \times 10^7$  viable cells  $\text{ml}^{-1}$ . After culturing of the conduits at 37°C for additional 7 days (a total of 10 days after seeding HUVMCs), hollow venous conduits, with a compact layer of endothelium covering the inner wall of the lumen and a thin, smooth muscle sheath across the outer surface, were eventually formed for downstream studies.

### Microfluidic extrusion bioprinting of dual-layered cellular conduits

BNSs with three coaxial channels were also used to bioprint dual-layered cellular tubular conduits. HUASMCs at 70 to 80% confluence were trypsinized, centrifuged, and resuspended in bioink at  $3 \times 10^7$  viable cells  $\text{ml}^{-1}$ . While MAlG1Gel15 was used for (bio) printing the inner layer, the LAlG2GM3 bioink was selected for the encapsulation and bioprinting of the outer HUASMC layer so as to facilitate growth and proliferation of these cells.  $\text{CaCl}_2$  solution (2%) flowing in the core facilitated the cross-linking of alginate in the bioink (Fig. 2A). The bioprinted dual-layered tubular conduits were later transferred into  $\text{CaCl}_2/\text{mTG}$  cross-linker prepared in SmGM-2 culture medium. After 12 hours of incubation at 37°C in the incubator, the cross-linker solution was replaced with fresh SmGM-2 culture medium. At 14 days of bioprinting, HUAECs were seeded in the lumen by perfusing 100 to 150  $\mu\text{l}$  of HUAEC suspension at  $1 \times 10^7$  viable cells  $\text{ml}^{-1}$ . After incubation of arterial conduits at 37°C for additional 7 days (thus a total of 24 days after bioprinting HUASMCs), hollow arterial conduits with a compact layer of endothelium covering the inner lumen wall and a thick smooth muscle sheath throughout the outer surface were eventually formed for downstream studies.

### Cell viability assay

Cell viability was measured by the Live/Dead viability/cytotoxicity kit according to the manufacturers' instructions. Briefly, the vascular conduits were washed with DPBS twice and placed in the wells of a six-well plate, followed by the addition of live/dead staining solution containing 4 mM of calcein acetoxymethyl (Calcein-AM) ( $1 \mu\text{l ml}^{-1}$ ) and 2 mM of ethidium homodimer-1 ( $2 \mu\text{l ml}^{-1}$ ) in DPBS. After incubation at 37°C for 30 min, the samples were washed three times with DPBS and observed under an Eclipse Ti2 inverted microscope (Nikon, NY, USA). Percentages of viable cells were determined using the ImageJ software.

### F-actin staining

For morphological analyses, Alexa Fluor 488-phalloidin or Alexa Fluor 549-phalloidin was used for F-actin staining. The vascular conduits were washed with deionized water twice and fixed with 4% (v/v) paraformaldehyde for 15 min. After gentle washing three times, the samples were permeabilized with 0.1% (v/v) Triton X-100 for 1 hour at room temperature. Alexa Fluor 488-phalloidin or Alexa Fluor 549-phalloidin [1:200 (v/v) in 0.1% BSA] was added to the samples and incubated for 1 hour at room temperature. The samples were washed again with deionized water and then stained with the DAPI [1:1000 (v/v) in DPBS] for 5 min at room

temperature. After washing three times with deionized water, fluorescence images were taken using a Zeiss LSM 880 confocal microscope (Zeiss, NY, USA).

### Immunostaining

The biofunctionalities of the endothelial and smooth muscle layers in the vein and arterial conduits were further confirmed by immunostaining of the cells for cell-specific markers including ZO-1, laminin,  $\alpha$ -SMA, and tubulin. The vascular conduits were fixed with 10% (v/v) formalin for 30 min at room temperature. After washing three times with deionized water, the samples were incubated with the permeabilization buffer [0.1% (v/v) Triton X-100 in deionized water] for 1 hour and blocked with 5% (v/v) goat serum in deionized water for 2 hours at room temperature. The samples were then incubated with the desired primary antibody (1:200 dilution in blocking buffer) overnight at 4°C. The samples were washed three times with deionized water and incubated overnight at 4°C with the relevant secondary antibody (Alexa Fluor 594-conjugated goat anti-rabbit secondary antibody or Alexa Fluor 488-conjugated goat anti-mouse secondary antibody) at 1:200 dilution in blocking buffer. Last, the nuclei were counterstained with DAPI after washing with deionized water and examined under the Zeiss LSM 880 confocal microscope.

### Vasoactivity assay

Phenylephrine-induced vasoconstriction and acetylcholine-induced vasodilation were assessed on arterial conduits. The drugs at given concentrations were prepared in the physiological salt solution composed of 123 mM of NaCl, 5 mM of KCl, 15.5 mM of  $\text{NaHCO}_3$ , 1.2 mM of  $\text{KH}_2\text{PO}_4$ , 1.2 mM of  $\text{MgCl}_2$ , 1.25 mM of  $\text{CaCl}_2$ , 11 mM of D-glucose, and 25 mM of Hepes at pH 7.40 adjusted with NaOH. Arterial conduits were first perfused with 10  $\mu\text{M}$  of phenylephrine to assess vasoconstriction responses. After 5 min, the vasodilation responses were assessed by adding 10  $\mu\text{M}$  of acetylcholine to the precontracted arterial conduits induced by phenylephrine. Phenylephrine-induced contraction and acetylcholine-induced dilation were examined under observed under the Eclipse Ti2 inverted microscope, and percentages of changes in the diameter were determined using ImageJ.

### pCoV-VPs production and infection of vascular conduits

Production of pCoV-VPs was carried out as described in our previous study (69). Briefly, human embryonic kidney 293T cells ( $5 \times 10^5$  cells  $\text{well}^{-1}$ ) were cultured in six-well plates for 24 hours at 37°C in the incubator and treated with 1.0  $\mu\text{g}$  of pCMV3-SARS-CoV2-Spike (Sino Biological, Chesterbrook, PA, USA), 1.0  $\mu\text{g}$  of pNL4-3 mCherry Luciferase (Addgene, MA, USA), and 0.5  $\mu\text{g}$  of pAdvantage (Promega, Madison, WI, USA) using the TransIT-X2 transfection reagent (Abcam, Waltham, MA, USA) to produce pCoV-VPs according to the manufacturer's instructions. After 48 hours, the supernatants containing pCoV-VPs were collected, centrifuged at 10,000g for 5 min to remove cell debris, and concentrated using a poly(ethylene glycol) virus precipitation kit (Abcam, Waltham, MA, USA) according to the manufacturer's instructions. pCoV-VPs were stored at 80°C until use.

To investigate pCoV-VP infection on vascular conduits and effects of model antiviral drugs, the samples were infected with pCoV-VPs at a multiplicity of infection of 0.5 in the presence of RMD (10  $\mu\text{M}$ ; MedKoo Biosciences, Morrisville, NC, USA) or ADQ (10  $\mu\text{M}$ ; Sigma-Aldrich, Burlington, MA, USA). After 48 hours of

infection, the mCherry-positive cells, which reflect the pCoV-VPs infections, were observed under the Eclipse Ti2 inverted microscope. Similarly, luciferase activity, which reflects the number of pCoV-VPs in the host cells, was measured after 48 hours of postinfection using the Luciferase assay system (Promega, Madison, WI, USA) according to the manufacturer's instructions. The infection values were calculated from the intensities measured for drug-treated samples divided by the average intensity measured for the control sample and multiplied by 100%.

The cytopathic effect of pCoV-VPs infections was assessed by the live/dead assay and the MTS assay using the CellTiter 96 Aqueous one solution cell proliferation assay kit (Promega, Madison, WI, USA) according to the manufacturer's instruction. Uninfected samples served as controls.

### Ex vivo and in vivo anastomose tests

For ex vivo connection tests, a (bio)printed small hydrogel conduit (1 mm in diameter) was anastomosed to a piece of mouse aorta by dropping fast-curing adhesive droplets (Newell Brands Inc., GA, USA) on the interface, while a larger conduit (5 mm in diameter) was connected to a piece of the human popliteal vein. The (bio)printed hydrogel conduits anastomosed with native mouse or human blood vessels were then perfused with fluorescent microbeads suspended in DPBS.

The in vivo anastomose tests were performed on three mice. Mice were anesthetized by isoflurane inhalation (5% induction and 2% maintenance). After careful incision and dissection, the vena cava was exposed, followed by closing the distal end and proximal end of the vein with vascular clamps, and the 2.5-cm segment was isolated to be cross-resected. A sterile (bio)printed vascular conduit was inserted into and stuck with the two exposed ends by adhesive glue. Clamps were then released and inspected for the flow of the blood through the anastomosed vascular conduits. After transplantation for each mouse, we kept monitoring the blood flow passing through the graft for 10 min without observing any noticeable leakage and then euthanized the animal.

### Statistical analyses

All the experiments were done in triplicates to quintuples for each data point and were repeated three to five times. Results were expressed as means  $\pm$  SEMs of three independent experiments, and statistical comparisons were performed using the one-way analysis of variance.  $P < 0.05$  was considered statistically significant.

### SUPPLEMENTARY MATERIALS

Supplementary material for this article is available at <https://science.org/doi/10.1126/sciadv.abq6900>

### REFERENCES AND NOTES

- C. Hwa, A. Sebastian, W. C. Aird, Endothelial biomedicine: Its status as an interdisciplinary field, its progress as a basic science, and its translational bench-to-bedside gap. *Endothelium* **12**, 139–151 (2005).
- S. P. Herbert, D. Y. R. Stainier, Molecular control of endothelial cell behaviour during blood vessel morphogenesis. *Nat. Rev. Mol. Cell Biol.* **12**, 551–564 (2011).
- W. D. Tucker, Y. Arora, K. Mahajan, *Anatomy, Blood Vessels* (StatPearls Publishing LLC, 2021).
- S. S. Virani, A. Alonso, H. J. Aparicio, E. J. Benjamin, M. S. Bittencourt, C. W. Callaway, A. P. Carson, A. M. Chamberlain, S. Cheng, F. N. Delling, M. S. V. Elkind, K. R. Evenson, J. F. Ferguson, D. K. Gupta, S. S. Khan, B. M. Kissela, K. L. Knutson, C. D. Lee, T. T. Lewis, J. Liu, M. S. Loop, P. L. Lutsey, J. Ma, J. Mackey, S. S. Martin, D. B. Matchar, M. E. Mussolino, S. D. Navaneethan, A. M. Perak, G. A. Roth, Z. Samad, G. M. Satou, E. B. Schroeder, S. H. Shah, C. M. Shay, A. Stokes, L. B. VanWagner, N. Y. Wang, C. W. Tsao; American Heart

- Association Council on Epidemiology and Prevention Statistics Committee and Stroke Statistics Subcommittee, Heart disease and stroke statistics-2021 update: A report from the American heart association. *Circulation* **143**, e254–e743 (2021).
- G. A. Roth, G. A. Mensah, C. O. Johnson, G. Addolorato, E. Ammirati, L. M. Baddour, N. C. Barengo, A. Z. Beaton, E. J. Benjamin, C. P. Benziger, A. Bonny, M. Brauer, M. Brodmann, T. J. Cahill, J. Carapetis, A. L. Catapano, S. S. Chugh, L. T. Cooper, J. Coresh, M. Criqui, N. DeCleene, K. A. Eagle, S. Emmons-Bell, V. L. Feigin, J. Fernández-Solà, G. Fowkes, E. Gakidou, S. M. Grundy, F. J. He, G. Howard, F. Hu, L. Inker, G. Karthikeyan, N. Kassebaum, W. Koroshetz, C. Lavie, D. Lloyd-Jones, H. S. Lu, A. Mirijello, A. M. Temesgen, A. Mokdad, A. E. Moran, P. Muntner, J. Narula, B. Neal, M. Ntsekhe, G. Moraes de Oliveira, C. Otto, M. Owolabi, M. Pratt, S. Rajagopalan, M. Reitsma, A. L. P. Ribeiro, N. Rigotti, A. Rodgers, C. Sable, S. Shakil, K. Sliwa-Hahnle, B. Stark, J. Sundström, P. Timpel, I. M. Tleyjeh, M. Valgimigli, T. Vos, P. K. Whelton, M. Yacoub, L. Zuhlke, C. Murray, V. Fuster; Global Burden of Cardiovascular Diseases and Risk Factors, Global burden of cardiovascular diseases and risk factors, 1990–2019. *J. Am. Coll. Cardiol.* **76**, 2982–3021 (2020).
  - L. D. Hillis, P. K. Smith, J. L. Anderson, J. A. Bittl, C. R. Bridges, J. G. Byrne, J. E. Cigarroa, V. J. DiSesa, L. F. Hiratzka, A. M. Hutter Jr., M. E. Jessen, E. C. Keeley, S. J. Lahey, R. A. Lange, M. J. London, M. J. Mack, M. R. Patel, J. D. Puskas, J. F. Sabik, O. Selnes, D. M. Shahian, J. C. Trost, M. D. Winniford, A. K. Jacobs, J. L. Anderson, N. Albert, M. A. Creager, S. M. Ettinger, R. A. Guyton, J. L. Halperin, J. S. Hochman, F. G. Kushner, E. M. Ohman, W. Stevenson, C. W. Yancy; American College of Cardiology Foundation/American Heart Association Task Force on Practice Guidelines, 2011 ACCF/AHA guideline for coronary artery bypass graft surgery: Executive summary: A report of the American College of Cardiology Foundation/American Heart Association Task Force on practice guidelines. *J. Thorac. Cardiovasc. Surg.* **143**, 4–34 (2012).
  - I. Ahmed, S. Yandrapalli, *Internal Mammary Artery Bypass* (StatPearls Publishing LLC, 2021).
  - P. Altschuler, P. Nahiriak, N. J. Welle, *Saphenous Vein Grafts* (StatPearls Publishing LLC, 2021).
  - STS data clarifies variables behind coronary artery bypass complication, mortality rates. *Data Strateg. Benchmarks* **2**, 172–174, 161 (1998).
  - A. L. Hawkes, M. Nowak, B. Bidstrup, R. Speare, Outcomes of coronary artery bypass graft surgery. *Vasc. Health Risk Manag.* **2**, 477–484 (2006).
  - B. McNichols, J. R. Spratt, J. George, S. Rizzi, E. W. Manning, K. Park, Coronary artery bypass: Review of surgical techniques and impact on long-term revascularization outcomes. *Cardiol. Ther.* **10**, 89–109 (2021).
  - J. G. Motwani, E. J. Topol, Aortocoronary saphenous vein graft disease. *Circulation* **97**, 916–931 (1998).
  - A. Malinska, Z. Podemska, B. Perek, M. Jemielny, P. Buczkowski, M. Grzymisławska, P. Sujka-Kordowska, M. Nowicki, Preoperative factors predicting saphenous vein graft occlusion in coronary artery bypass grafting: A multivariate analysis. *Histochem. Cell Biol.* **148**, 417–424 (2017).
  - A. Lejay, V. Vento, S. Kuntz, L. Steinmetz, Y. Georg, F. Thaveau, F. Heim, N. Chakfé, Current status on vascular substitutes. *J. Cardiovasc. Surg. (Torino)* **61**, 538–543 (2020).
  - H.-H. Greco Song, R. T. Rumma, C. K. Ozaki, E. R. Edelman, C. S. Chen, Vascular tissue engineering: Progress, challenges, and clinical promise. *Cell Stem Cell* **22**, 340–354 (2018).
  - M. D. Sarker, S. Naghieh, N. K. Sharma, L. Ning, X. Chen, Bioprinting of vascularized tissue scaffolds: Influence of biopolymer, cells, growth factors, and gene delivery. *J. Healthc. Eng.* **2019**, 9156921 (2019).
  - X. Cao, S. Maharjan, R. Ashfaq, J. Shin, Y. S. Zhang, Bioprinting of small-diameter blood vessels. *Engineering* **7**, 832–844 (2021).
  - P. Sasmal, P. Datta, Y. Wu, I. T. Ozbolat, 3D bioprinting for modelling vasculature. *Microphysiol. Syst.* **2**, 9 (2018).
  - Y. S. Zhang, G. Haghiashtiani, T. Hübscher, D. J. Kelly, J. M. Lee, M. Lutolf, M. C. McAlpine, W. Y. Yeong, M. Zenobi-Wong, J. Malda, 3D extrusion bioprinting. *Nat. Rev. Methods Primers* **1**, 75 (2021).
  - D. N. d. Chatinier, K. P. Figler, P. Agrawal, W. Liu, Y. S. Zhang, The potential of microfluidics-enhanced extrusion bioprinting. *Biomicrofluidics* **15**, 041304 (2021).
  - M. Costantini, C. Colosi, W. Świążkowski, A. Barbeta, Co-axial wet-spinning in 3D bioprinting: State of the art and future perspective of microfluidic integration. *Biofabrication* **11**, 012001 (2019).
  - S. Hong, S. K. Ji, B. Jung, C. Won, C. Hwang, Coaxial bioprinting of cell-laden vascular constructs using a gelatin-tyramine bioink. *Biomater. Sci.* **7**, 4578–4587 (2019).
  - L. Andrique, G. Recher, K. Alessandri, N. Pujol, M. Feyeux, P. Bon, L. Cognet, P. Nassyoy, A. Bikfalvi, A model of guided cell self-organization for rapid and spontaneous formation of functional vessels. *Sci. Adv.* **5**, eaau6562 (2019).
  - G. Gao, J. Y. Park, B. S. Kim, J. Jang, D.-W. Cho, Coaxial cell printing of freestanding, perfusable, and functional in vitro vascular models for recapitulation of native vascular endothelium pathophysiology. *Adv. Healthc. Mater.* **7**, 1801102 (2018).
  - G. Gao, W. Park, B. S. Kim, M. Ahn, S. Chae, W.-W. Cho, J. Kim, J. Y. Lee, J. Jang, D.-W. Cho, Construction of a novel in vitro atherosclerotic model from geometry-tunable artery

- equivalents engineered via in-bath coaxial cell printing. *Adv. Funct. Mater.* **31**, 2008878 (2021).
26. W. Jia, P. S. Gungor-Ozkerim, Y. S. Zhang, K. Yue, K. Zhu, W. Liu, Q. Pi, B. Byambaa, M. R. Dokmeci, S. R. Shin, A. Khademhosseini, Direct 3D bioprinting of perfusable vascular constructs using a blend bioink. *Biomaterials* **106**, 58–68 (2016).
  27. Q. Pi, S. Maharjan, X. Yan, X. Liu, B. Singh, A. M. van Genderen, F. Robledo-Padilla, R. Parra-Saldivar, N. Hu, W. Jia, C. Xu, J. Kang, S. Hassan, H. Cheng, X. Hou, A. Khademhosseini, Y. S. Zhang, Digitally tunable microfluidic bioprinting of multilayered cannular tissues. *Adv. Mat.* **30**, e1706913 (2018).
  28. Q. Liang, F. Gao, Z. Zeng, J. Yang, M. Wu, C. Gao, D. Cheng, H. Pan, W. Liu, C. Ruan, Coaxial scale-up printing of diameter-tunable biohybrid hydrogel microtubes with high strength, perfusability, and endothelialization. *Adv. Funct. Mater.* **30**, 2001485 (2020).
  29. Y. Zhang, Y. Yu, A. Akkouch, A. Dababneh, F. Dolati, I. T. Ozbolat, In vitro study of directly bioprinted perfusable vasculature conduits. *Biomater. Sci.* **3**, 134–143 (2015).
  30. J. P. Gong, Y. Katsuyama, T. Kurokawa, Y. Osada, Double-network hydrogels with extremely high mechanical strength. *Adv. Mat.* **15**, 1155–1158 (2003).
  31. X. Zhao, X. Chen, H. Yuk, S. Lin, X. Liu, G. Parada, Soft materials by design: Unconventional polymer networks give extreme properties. *Chem. Rev.* **121**, 4309–4372 (2021).
  32. N. Contessi Negri, A. Angelova Volponi, P. T. Sharpe, A. D. Celiz, Tunable cross-linking and adhesion of gelatin hydrogels via bioorthogonal click chemistry. *ACS Biomater. Sci. Eng.* **7**, 4330–4346 (2021).
  33. C. W. Yung, L. Q. Wu, J. A. Tullman, G. F. Payne, W. E. Bentley, T. A. Barbari, Transglutaminase crosslinked gelatin as a tissue engineering scaffold. *J. Biomed. Mater. Res.* **A 83**, 1039–1046 (2007).
  34. J. P. Gong, Why are double network hydrogels so tough? *Soft Matter* **6**, 2583–2590 (2010).
  35. O. Chaudhuri, L. Gu, D. Klumpers, M. Darnell, S. A. Bencherif, J. C. Weaver, N. Huebsch, H.-p. Lee, E. Lippens, G. N. Duda, D. J. Mooney, Hydrogels with tunable stress relaxation regulate stem cell fate and activity. *Nat. Mater.* **15**, 326–334 (2016).
  36. J. Li, Y. Wu, J. He, Y. Huang, A new insight to the effect of calcium concentration on gelation process and physical properties of alginate films. *J. Mater. Sci.* **51**, 5791–5801 (2016).
  37. B. G. Compton, J. A. Lewis, 3D-printing of lightweight cellular composites. *Adv. Mat.* **26**, 5930–5935 (2014).
  38. S. A. Ghodbane, N. S. Murthy, M. G. Dunn, J. Kohn, Achieving molecular orientation in thermally extruded 3D printed objects. *Biofabrication* **11**, 045004 (2019).
  39. J. L. Drury, R. G. Dennis, D. J. Mooney, The tensile properties of alginate hydrogels. *Biomaterials* **25**, 3187–3199 (2004).
  40. S. K. Burke, K. Bingham, E. Moss, D. P. Gottlieb, M. D. Wong, K. S. Bland, F. N. Franano, Recombinant human elastase alters the compliance of atherosclerotic tibial arteries after ex vivo angioplasty. *J. Cardiovasc. Pharmacol.* **67**, 305–311 (2016).
  41. J. Gavard, Endothelial permeability and VE-cadherin: A wacky comradeship. *Cell Adh. Migr.* **7**, 455–461 (2013).
  42. W. Liu, Z. Zhong, N. Hu, Y. Zhou, L. Maggio, A. K. Miri, A. Fragasso, X. Jin, A. Khademhosseini, Y. S. Zhang, Coaxial extrusion bioprinting of 3D microfibrous constructs with cell-favorable gelatin methacryloyl microenvironments. *Biofabrication* **10**, 024102 (2018).
  43. S. Pashneh-Tala, S. MacNeil, F. Claeysens, The tissue-engineered vascular graft-past, present, and future. *Tissue Eng. Part B Rev.* **22**, 68–100 (2016).
  44. "Structure and function of blood vessels"; <https://courses.lumenlearning.com/suny-ap2/chapter/structure-and-function-of-blood-vessels/>.
  45. A. Banerjee, M. Arha, S. Choudhary, R. S. Ashton, S. R. Bhatia, D. V. Schaffer, R. S. Kane, The influence of hydrogel modulus on the proliferation and differentiation of encapsulated neural stem cells. *Biomaterials* **30**, 4695–4699 (2009).
  46. M. J. Davis, M. A. Hill, Signaling mechanisms underlying the vascular myogenic response. *Physiol. Rev.* **79**, 387–423 (1999).
  47. M. A. Hill, G. A. Meininger, M. J. Davis, I. Laher, Therapeutic potential of pharmacologically targeting arteriolar myogenic tone. *Trends Pharmacol. Sci.* **30**, 363–374 (2009).
  48. K. F. Franzen, M. Meusel, J. Engel, T. Röcker, D. Drömann, F. Sayk, Differential effects of Angiotensin-II compared to phenylephrine on arterial stiffness and hemodynamics: A placebo-controlled study in healthy humans. *Cells* **10**, 1108 (2021).
  49. H. B. Nguyen, S. Y. Lee, S. H. Park, M. Y. Lee, I. H. Chang, S. C. Myung, Relaxing effect of acetylcholine on phenylephrine-induced contraction of isolated rabbit prostate strips is mediated by neuronal nitric oxide synthase. *Korean J. Urol.* **54**, 333–338 (2013).
  50. "COVID-19 dashboard by the Center for Systems Science and Engineering (CSSE) at Johns Hopkins University (JHU)"; <https://coronavirus.jhu.edu/map.html>.
  51. C. B. Jackson, M. Farzan, B. Chen, H. Choe, Mechanisms of SARS-CoV-2 entry into cells. *Nat. Rev. Mol. Cell Biol.* **23**, 3–20 (2022).
  52. K. Katella, "Omicron, delta, alpha, and more: What to know about the coronavirus variants" (Yale Medicine, 2022); [www.yalemedicine.org/news/covid-19-variants-of-concern-omicron](http://www.yalemedicine.org/news/covid-19-variants-of-concern-omicron).
  53. S. K. Abrokwa, S. A. Müller, A. Méndez-Brito, J. Hanefeld, C. El Bcheraoui, Recurrent SARS-CoV-2 infections and their potential risk to public health - A systematic review. *PLOS ONE* **16**, e0261221 (2021).
  54. R. Rauti, M. Shahoha, Y. Leichtmann-Bardoogo, R. Nasser, E. Paz, R. Tamir, V. Miller, T. Babich, K. Shaked, A. Ehrlich, K. Ioannidis, Y. Nahmias, R. Sharan, U. Ashery, B. M. Maoz, Effect of SARS-CoV-2 proteins on vascular permeability. *eLife* **10**, e69314 (2021).
  55. L. C. Barbosa, T. L. Gonçalves, L. P. de Araujo, L. V. de Oliveira Rosario, V. P. Ferrer, Endothelial cells and SARS-CoV-2: An intimate relationship. *Vascul. Pharmacol.* **137**, 106829 (2021).
  56. COVID-19 and vascular disease. *EBioMedicine* **58**, 102966 (2020).
  57. A. J. Pruijssers, A. S. George, A. Schäfer, S. R. Leist, L. E. Gralinski, K. H. Dinno III, B. L. Yount, M. L. Agostini, L. J. Stevens, J. D. Chappell, X. Lu, T. M. Hughes, K. Gully, D. R. Martinez, A. J. Brown, R. L. Graham, J. K. Perry, V. D. Pont, J. Pitts, B. Ma, D. Babusis, E. Murakami, J. Y. Feng, J. P. Billelo, D. P. Porter, T. Cihlar, R. S. Baric, M. R. Denison, T. P. Sheahan, Remdesivir inhibits SARS-CoV-2 in human lung cells and chimeric SARS-CoV expressing the SARS-CoV-2 RNA polymerase in mice. *Cell Rep.* **32**, 107940 (2020).
  58. S. Weston, C. M. Coleman, R. Haupt, J. Logue, M. B. Frieman, Broad anti-coronavirus activity of Food and Drug Administration-approved drugs against SARS-CoV-2 *in vitro* and SARS-CoV *in vivo*. *J. Virol.* **94**, e01218–e01220 (2020).
  59. C. L. Onweni, Y. S. Zhang, T. Caulfield, C. E. Hopkins, D. L. Fairweather, W. D. Freeman, ACEI/ARB therapy in COVID-19: The double-edged sword of ACE2 and SARS-CoV-2 viral docking. *Crit. Care* **24**, 475 (2020).
  60. A. G. Harrison, T. Lin, P. Wang, Mechanisms of SARS-CoV-2 transmission and pathogenesis. *Trends Immunol.* **41**, 1100–1115 (2020).
  61. J. Gong, C. C. L. Schuurmans, A. M. van Genderen, X. Cao, W. Li, F. Cheng, J. J. He, A. López, V. Huerta, J. Manríquez, R. Li, H. Li, C. Delavaux, S. Sebastian, P. E. Capendale, H. Wang, J. Xie, M. Yu, R. Masereeuw, T. Vermonden, Y. S. Zhang, Complexation-induced resolution enhancement of 3D-printed hydrogel constructs. *Nat. Commun.* **11**, 1267 (2020).
  62. S. Maharjan, J. Alva, C. Cámara, A. G. Rubio, D. Hernández, C. Delavaux, E. Correa, M. D. Romo, D. Bonilla, M. L. Santiago, W. Li, F. Cheng, G. Ying, Y. S. Zhang, Symbiotic photosynthetic oxygenation within 3D-bioprinted vascularized tissues. *Matter* **4**, 217–240 (2021).
  63. H. Ravanbakhsh, Z. Luo, X. Zhang, S. Maharjan, H. S. Mirkarimi, G. Tang, C. Chávez-Madero, L. Mongeau, Y. S. Zhang, Freeform cell-laden cryobioprinting for shelf-ready tissue fabrication and storage. *Matter* **5**, 573–593 (2022).
  64. H. Han, Y. Park, Y.-M. Choi, Y. Yong, B. Kang, W. Shin, S. Min, H. J. Kim, J. Jang, A bioprinted tubular intestine model using a colon-specific extracellular matrix bioink. *Adv. Healthc. Mater.* **11**, 2101768 (2022).
  65. C. Xiang, Z. Wang, C. Yang, X. Yao, Y. Wang, Z. Suo, Stretchable and fatigue-resistant materials. *Mater. Today* **34**, 7–16 (2020).
  66. S. Massa, M. A. Sakr, J. Seo, P. Bandaru, A. Arneri, S. Bersini, E. Zare-Eelanjegh, E. Jalilian, B.-H. Cha, S. Antona, A. Enrico, Y. Gao, S. Hassan, J. P. Acevedo, M. R. Dokmeci, Y. S. Zhang, A. Khademhosseini, S. R. Shin, Bioprinted 3D vascularized tissue model for drug toxicity analysis. *Biomicrofluidics* **11**, 044109 (2017).
  67. D. B. Kolesky, K. A. Homan, M. A. Skylar-Scott, J. A. Lewis, Three-dimensional bioprinting of thick vascularized tissues. *Proc. Natl. Acad. Sci. U.S.A.* **113**, 3179–3184 (2016).
  68. D. Wang, W. Chen, Indocyanine green angiography for continuously monitoring blood flow changes and predicting perfusion of deep inferior epigastric perforator flap in rats. *J. Invest. Surg.* **34**, 393–400 (2021).
  69. D. Huang, T. Liu, J. Liao, S. Maharjan, X. Xie, M. Pérez, I. Anaya, S. Wang, A. Tirado Mayer, Z. Kang, W. Kong, V. L. Mainardi, C. E. Garciamendez-Mijares, G. García Martínez, M. Moretti, W. Zhang, Z. Gu, A. M. Ghaemmaghami, Y. S. Zhang, Reverse-engineered human alveolar lung-on-a-chip model. *Proc. Natl. Acad. Sci. U.S.A.* **118**, e2016146118 (2021).
  70. Q. Gao, Y. He, J.-Z. Fu, A. Liu, L. Ma, Coaxial nozzle-assisted 3D bioprinting with built-in microchannels for nutrients delivery. *Biomaterials* **61**, 203–215 (2015).
  71. G. Gao, J. H. Lee, J. Jang, D. H. Lee, J.-S. Kong, B. S. Kim, Y.-J. Choi, W. B. Jang, Y. J. Hong, S.-M. Kwon, D.-W. Cho, Tissue engineered bio-blood-vessels constructed using a tissue-specific bioink and 3D coaxial cell printing technique: A novel therapy for ischemic disease. *Adv. Funct. Mater.* **27**, 1700798 (2017).
  72. G. Gao, H. Kim, B. S. Kim, J. S. Kong, J. Y. Lee, B. W. Park, S. Chae, J. Kim, K. Ban, J. Jang, H.-J. Park, D.-W. Cho, Tissue-engineering of vascular grafts containing endothelium and smooth-muscle using triple-coaxial cell printing. *Appl. Phys. Rev.* **6**, 041402 (2019).
  73. S. C. Millik, A. M. Dostie, D. G. Karis, P. T. Smith, M. McKenna, N. Chan, C. D. Curtis, E. Nance, A. B. Theberge, A. Nelson, 3D printed coaxial nozzles for the extrusion of hydrogel tubes toward modeling vascular endothelium. *Biofabrication* **11**, 045009 (2019).
  74. L. Shao, Q. Gao, C. Xie, J. Fu, M. Xiang, Y. He, Directly coaxial 3D bioprinting of large-scale vascularized tissue constructs. *Biofabrication* **12**, 035014 (2020).

**Acknowledgments**

**Funding:** We acknowledge support by the National Institutes of Health (R01HL153857) and the Brigham Research Institute. We further thank D. A. Weitz's team from Harvard University and the NeuroTechnology Studio at Brigham and Women's Hospital for providing instrument access and data analyses. **Author contributions:** Conceptualization: Y.S.Z. Methodology: D.W., S.M., X.K., L.S.M., M.T., P.Y., X.C., L.Li., L. Lv, J.J.H., G.T., and H.Y. Visualization: Z.W. and L.S.M. Supervision: Y.S.Z., X.Z., and C.K.O. Writing—original draft: D.W., S.M., and X.K. Writing—review and editing: Y.S.Z., X.Z., C.K.O., D.W., S.M., and X.K. **Competing interests:** Y.S.Z. sits on the Scientific Advisory Board of Allevi by 3D Systems, which, however, did not sponsor or bias the current research. A provisional patent resulting from the work has been filed by the Brigham and Women's Hospital (filed 26 July 2022). The authors declare that they have no

other competing interests. **Data and materials availability:** All data needed to evaluate the conclusions in the study are present in the paper and/or the Supplementary Materials. The (bio)inks related to this study are available from the corresponding authors upon reasonable request pending scientific review and a completed material transfer agreement. Requests for the (bio)inks should be submitted to Mass General Brigham Innovation Team (innovations@partners.org).

Submitted 25 April 2022

Accepted 17 August 2022

Published 26 October 2022

10.1126/sciadv.abq6900

## Microfluidic bioprinting of tough hydrogel-based vascular conduits for functional blood vessels

Di WangSushila MaharjanXiao KuangZixuan WangLuis S. MilleMing TaoPeng YuXia CaoLiming LianLi LvJacqueline Jialu HeGuosheng TangHyunwoo YukC. Keith OzakiXuanhe ZhaoYu Shrike Zhang

*Sci. Adv.*, 8 (43), eabq6900. • DOI: 10.1126/sciadv.abq6900

### View the article online

<https://www.science.org/doi/10.1126/sciadv.abq6900>

### Permissions

<https://www.science.org/help/reprints-and-permissions>

Use of this article is subject to the [Terms of service](#)

---

*Science Advances* (ISSN ) is published by the American Association for the Advancement of Science. 1200 New York Avenue NW, Washington, DC 20005. The title *Science Advances* is a registered trademark of AAAS.

Copyright © 2022 The Authors, some rights reserved; exclusive licensee American Association for the Advancement of Science. No claim to original U.S. Government Works. Distributed under a Creative Commons Attribution NonCommercial License 4.0 (CC BY-NC).

Supplementary Materials for  
**Microfluidic bioprinting of tough hydrogel-based vascular conduits for  
functional blood vessels**

Di Wang *et al.*

Corresponding author: Yu Shrike Zhang, yszhang@research.bwh.harvard.edu; Xuanhe Zhao, zhaox@mit.edu;  
C. Keith Ozaki, ckozaki1@bwh.harvard.edu

*Sci. Adv.* **8**, eabq6900 (2022)  
DOI: 10.1126/sciadv.abq6900

**The PDF file includes:**

Figs. S1 to S16  
Table S1  
Legends for movies S1 to S6  
References

**Other Supplementary Material for this manuscript includes the following:**

Movies S1 to S6

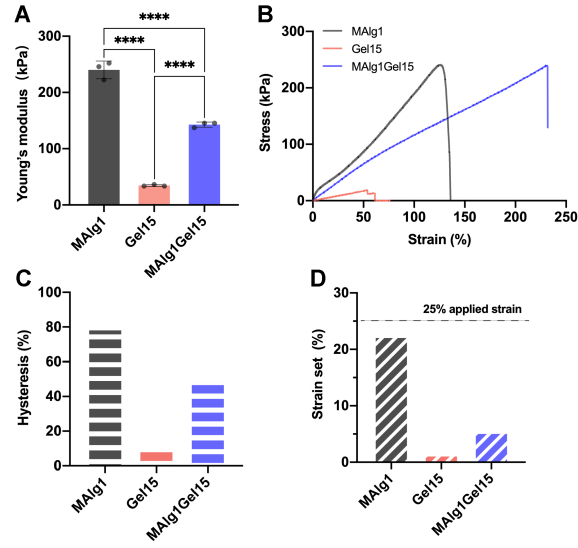


**Fig. S1.** Effect of components on DN hydrogel mechanical properties. **(A)** Young's moduli, **(B)** Uniaxial tensile stress–strain curves, **(C)** hysteresis ratios, and **(D)** strain sets after applying a maximum strain of 25% for MAIg1, Gel15, and MAIg1Gel15. \*\*\*\* $p < 0.0001$ .

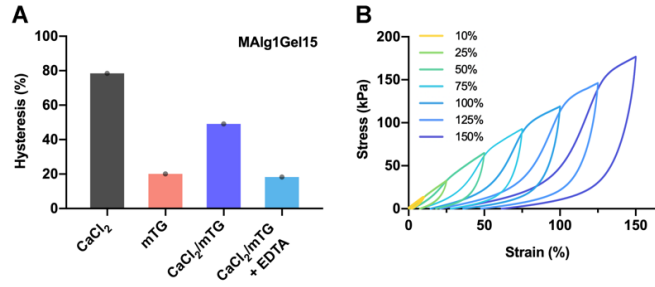


**Fig. S2.** Effect of curing conditions on DN hydrogel mechanical properties. **(A)** Hysteresis ratio of hybrid hydrogel (MAIg1Gel15) with different curing conditions and post-treatment. **(B)** Successive loading–unloading stress–strain curves of MAIg1Gel15 DN hydrogel with different maximum applied strains from 10% to 150%.

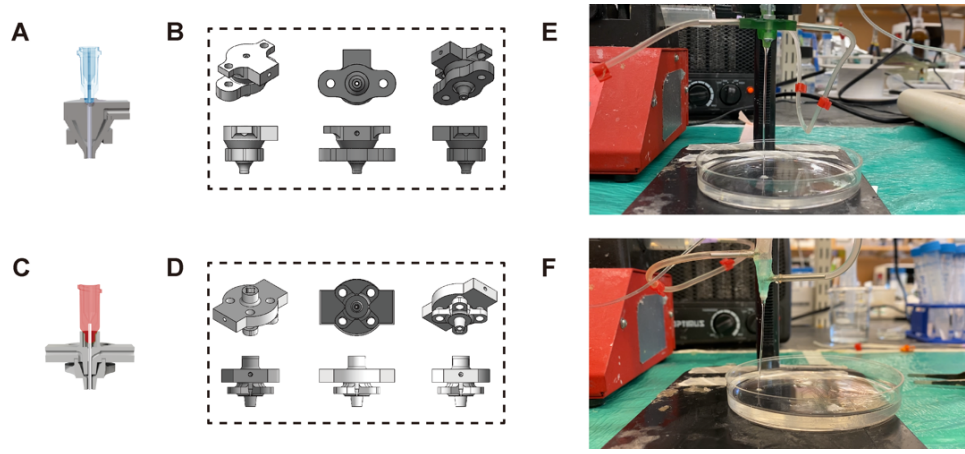


**Fig. S3.** Two types of multichannel coaxial extrusion systems. **(A)** General view of the two-channel nozzle for (bio)printing of mono-layered tubes. **(B)** Additional views of the two-channel nozzle. **(C)** General view of three-channel nozzle for (bio)printing of dual-layered tubes. **(D)** Additional views of the three-channel nozzle. Vascular conduit printing using **(E)** a coaxial extrusion nozzle assembled assisted by the 3D-printed BNS, and **(F)** a coaxial extrusion nozzle made entirely from commercial needles.

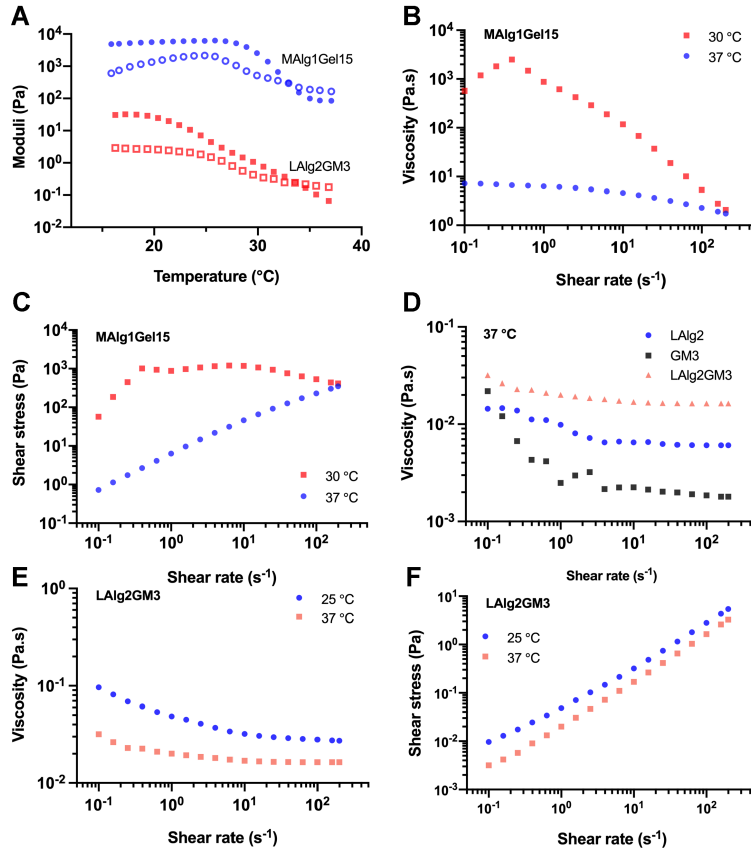


**Fig. S4.** Rheological measurements of the two hybrid (bio)inks. **(A)** Storage moduli (solid marks) and loss moduli (open marks) as a function of temperature for the two different (bio)inks. **(B)** Apparent viscosities and **(C)** shear stresses of the hybrid (bio)ink MAIg1Gel15 as a function of shear rate at 30 and 37 °C measured by flow-sweep. **(D)** Apparent viscosities of LAIg2, GM3, and LAIg2GM3 as a function of shear rate at 37 °C. **(E)** Apparent viscosities and **(F)** shear stresses of the hybrid (bio)ink of LAIg2GM3 as a function of shear rate at 25 and 37 °C measured by flow-sweep.

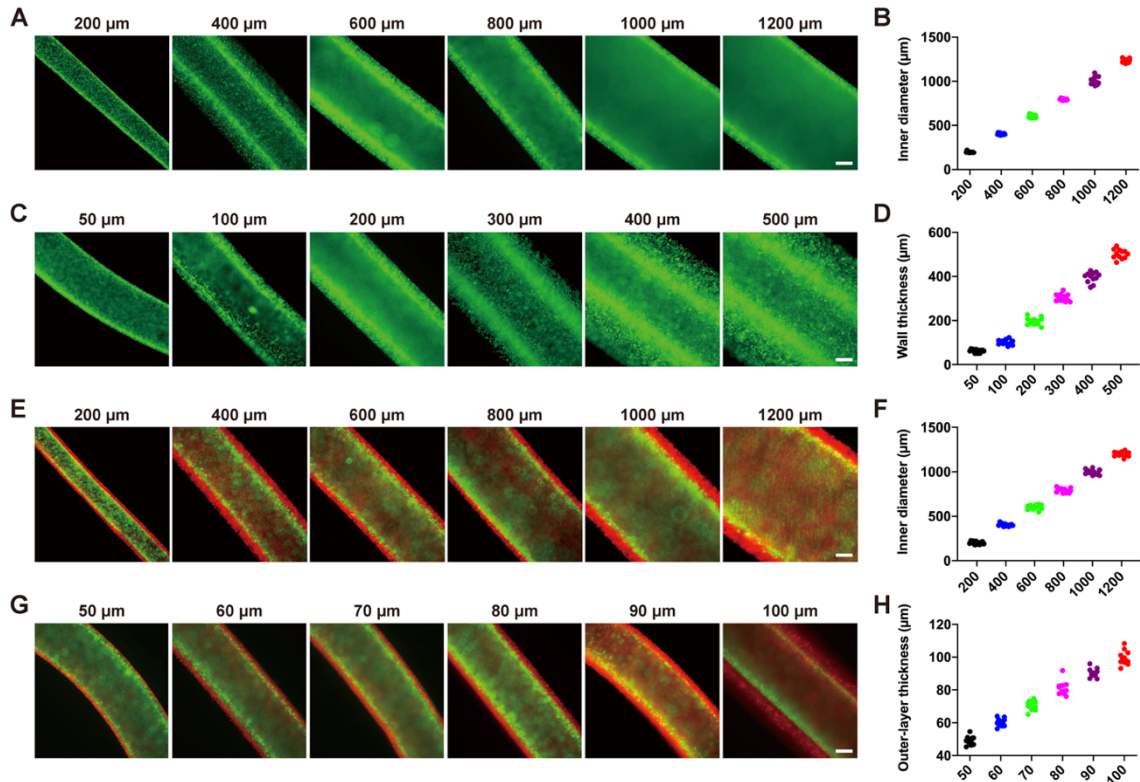


**Fig. S5.** Demonstration of (bio)printed size-tunable vascular acellular conduits. **(A)** Diameter-tunable mono-layered conduits. **(B)** Inner diameter of mono-layered conduits. **(C)** Wall thickness-tunable mono-layered conduits. **(D)** Wall thickness of mono-layered conduits. **(E)** Diameter-tunable dual-layered conduits. **(F)** Inner diameter of dual-layered conduits. **(G)** Wall thickness-tunable dual-layered conduits. **(H)** Outer-layer thickness of dual-layered conduits. Scale bars, 200  $\mu\text{m}$ .

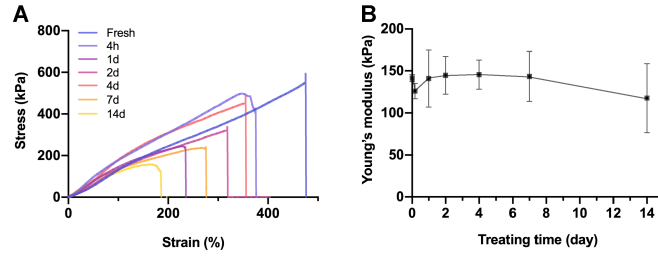


**Fig. S6.** Mechanical properties of (bio)printed MAlGel15 tubes after treatment with SMC culture medium at 37 °C. **(A)** Tensile stress–strain curves and **(B)** Young’s moduli of (bio)printed tubes after treatment in SMC culture medium for different times.

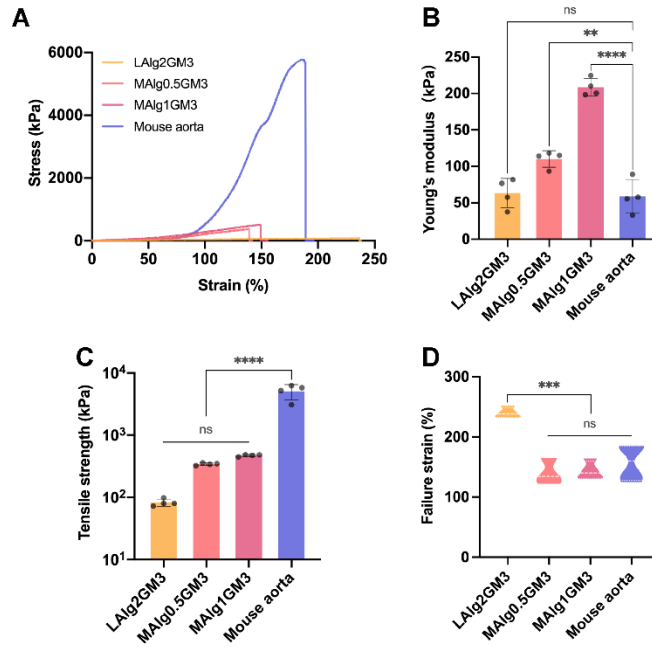


**Fig. S7.** Comparisons of mechanical properties of the (bio)printed dual-layered vascular tubes with different (bio)inks and the mouse aorta: **(A)** tensile stress–strain curves, **(B)** Young’s moduli, **(C)** tensile strengths, and **(D)** failure strains. ns: no significant difference, \*\* $p < 0.01$ , \*\*\* $p < 0.001$ , \*\*\*\* $p < 0.0001$ .

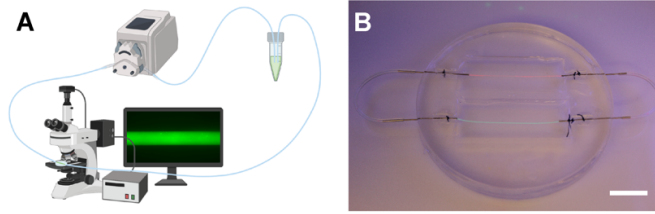


**Fig. S8.** The circulation and bioreactor setup for diffusion tests. **(A)** Schematic of the circulation system including a peristaltic pump connected to a tube containing FITC-Dex solution perfused through the chip-fitted vascular conduit, observed under a microscope. **(B)** Photograph of a two-channel bioreactor with two (bio)printed conduits connected. Scale bar, 2 cm.

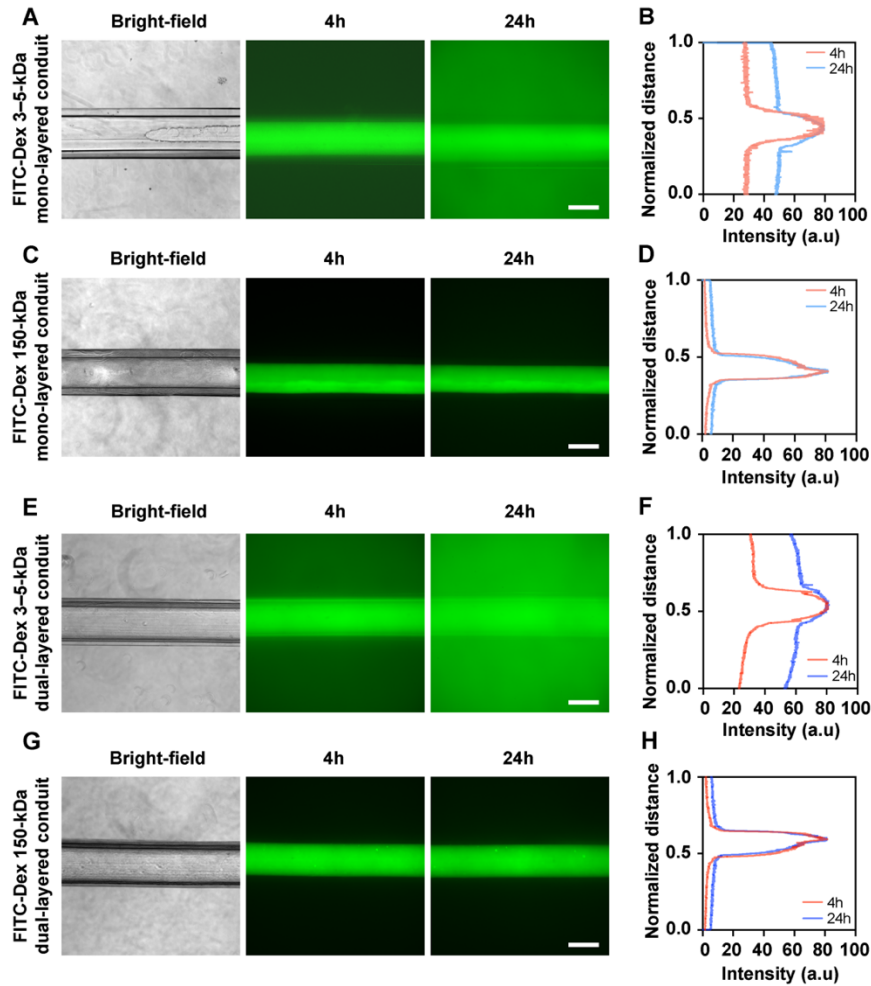


**Fig. S9.** Diffusion and permeability measurements of (bio)printed mono-layered and dual-layered conduits. (A, C) Bright-field and fluorescence images and (B, D) fluorescence intensity profiles of 3–5-kDa and 150-kDa FITC-Dex permeability tests in mono-layered conduits. (E, G) Bright-field and fluorescence images and (F, H) fluorescence intensity profiles of 3–5-kDa and 150-kDa FITC-Dex permeability tests in dual-layered conduits. Scale bars, 500  $\mu\text{m}$ .

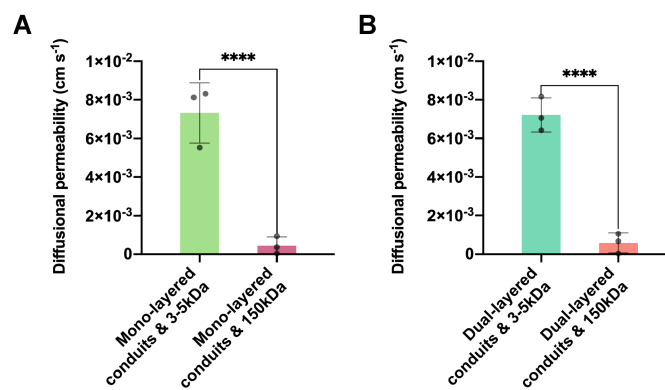


**Fig. S10.** Quantified diffusional permeability of small- and large- $M_w$  fluorescence molecules. Diffusional permeability values in **(A)** mono-layered conduits and **(B)** dual-layered conduits. \*\*\*\* $p < 0.0001$ .

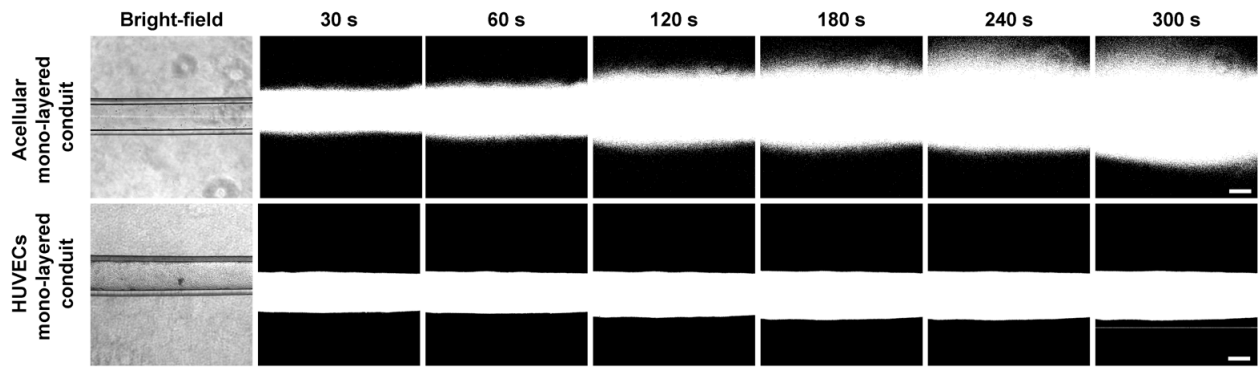


**Fig. S11.** Diffusion profiles of 3–5-kDa FITC-Dex from (bio)printed mono-layered conduits with and without HUVEC layer in the lumen at selected time points. Scale bars, 200  $\mu\text{m}$ .

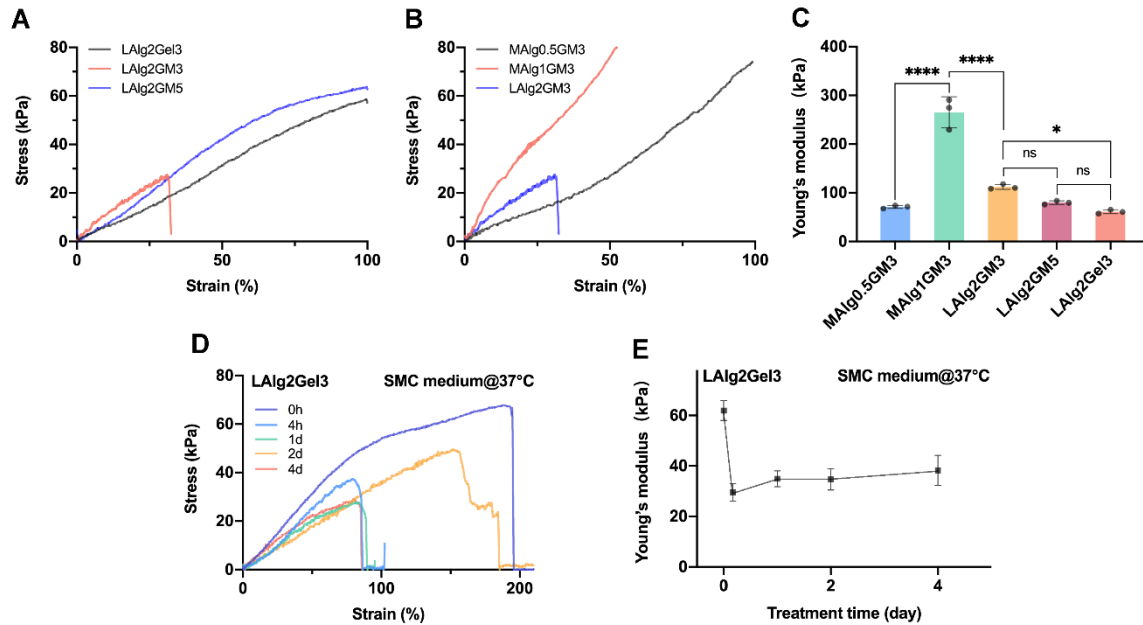


**Fig. S12.** Mechanical properties of (bio)printed acellular mono-layered tubes featuring different outer-layer (bio)inks. Tensile stress–strain curves of **(A)** (bio)printed tubes consisting of 2% low-viscosity alginate and different contents of GelMA or gelatin, and **(B)** (bio)printed tubes consisting of 3% GelMA and different types and contents of alginate. **(C)** Young's moduli of all the samples in (A) and (B). **(D)** Tensile stress–strain curves and **(E)** Young's modulus variations of (bio)printed LAlg2Gel3 tubes immersed in SMC medium at 37 °C for indicated times. ns: no significant difference, \* $p < 0.05$ , \*\*\*\* $p < 0.0001$ .

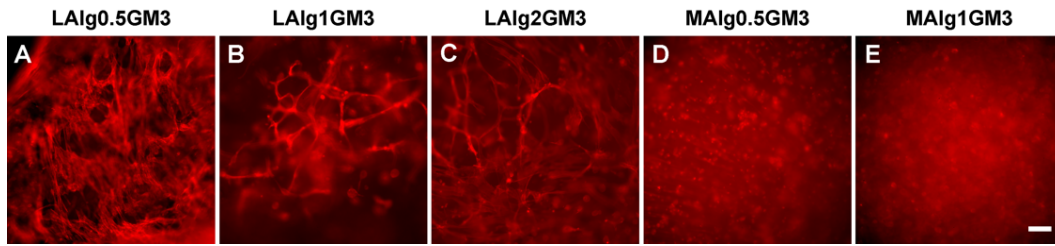


**Fig. S13.** F-actin staining of encapsulated HUASMCs in different bioinks at day 7. (A) LAIg0.5GM3, (B) LAIg1GM3, (C) LAIg2GM3, (D) MAIg0.5GM3, and (E) MAIg1GM3 bioinks. Scale bars, 100  $\mu\text{m}$ .

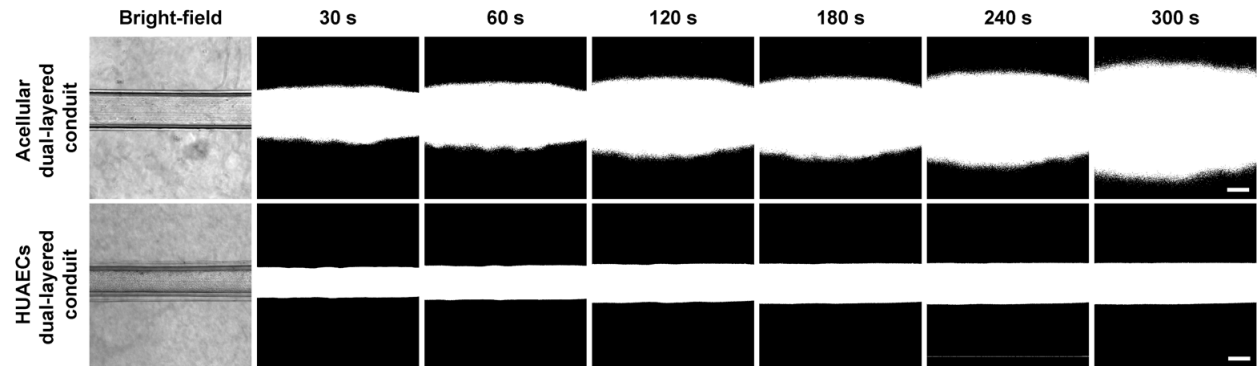


**Fig. S14.** Diffusion profiles of 3–5-kDa FITC-Dex across the walls of the (bio)printed dual-layered conduits in the absence (top) and the presence (bottom) of HUAEC layer in the lumen at selected time points. Scale bars, 200  $\mu\text{m}$ .

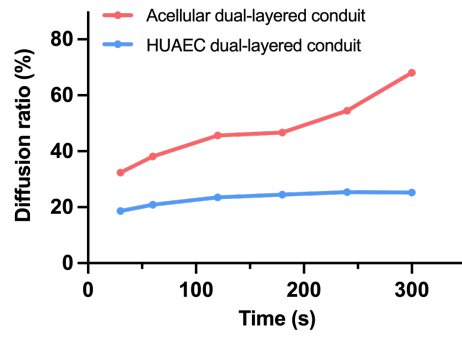


**Fig. S15.** Quantified diffusion ratios of 3–5-kDa FITC-Dex as a function of time in the absence and presence of HUAEC layer in the lumen of dual-layered conduits.

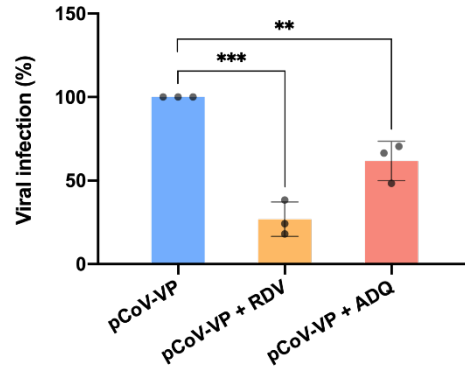


**Fig. S16.** Quantified infections of the venous conduits with pCoV-VPs. \*\* $p < 0.01$ , \*\*\* $p < 0.001$ .

**Table S1.** Comparisons of mechanical and biological performances for (bio)printed vascular conduits.

Materials	Young's Modulus (kPa)	Ultimate Tensile Strength (kPa)	Failure Strain (%)	Burst Pressure (mmHg)	Perfusability	Barrier Performance	Vasoactivity	Biomarker Expressions	Applications	Study*
Alginate	105–341	110–382	69–82	43–303	Yes	Yes	-	-	-	Zhang 2015 (29)
Alginate	-	46–116	155–96	-	Yes	Yes	-	-	-	Gao 2015 (70)
GelMA, alginate, PEGTA, VdECM,	24–51	-	-	-	Yes	-	-	CD31, $\alpha$ -SMA	-	Jia 2016 (26)
alginate, PLGA microspheres	-	-	-	-	Yes	-	-	CD31, $\alpha$ -SMA	<i>In vivo</i> grafts, <i>in vitro</i> models	Gao 2017 (71)
VdECM, alginate	-	-	-	-	Yes	Yes	-	CD31, VE-cadherin, laminin	<i>In vitro</i> models	Gao 2018 (24)
GelMA, alginate, PEGOA	≈12	-	-	-	Yes	-	-	ZO-1, VE-cadherin, $\alpha$ -SMA, VE-cadherin	-	Pi 2018 (27)
VdECM, alginate	-	47–195	-	63–174	Yes	-	Contraction	Elastin, R-COL-1, H-COL-1, H- $\alpha$ -SMA, CD31	<i>In vivo</i> grafts	Gao 2019 (72)
Gelatin, PEG, tyramine	-	-	-	-	-	-	-	-	-	Hong 2019 (22)
Alginate	-	-	-	-	Yes	Yes	Contraction	$\alpha$ -SMA, CD31, Laminin, Tubulin	-	Andrique 2019 (23)
F127, BUM	-	-	-	-	Yes	-	-	CD31	-	Millik 2019 (73)
VdECM, alginate	-	-	-	-	Yes	Yes	-	$\alpha$ -SMA, CD31, H-COL-1	<i>In vitro</i> models	Gao 2021 (25)
GelMA, nanoclay, NAGA	≈21,000	≈22,000	≈500	≈2,500	Yes	Yes	-	CD31, vWF	-	Liang 2020 (28)
GelMA, gelatin	1–6	-	-	-	-	-	-	CD31	<i>In vitro</i> models	Shao 2020 (74)
Alginate, gelatin (or GelMA)	171 (mono-layered), 63 (dual-layered)	538 (mono-layered), 82 (dual-layered)	184 (mono-layered), 240 (dual-layered)	1,113–1,498 (mono-layered), 1,138 (dual-layered)	Yes	Yes	Contraction, Dilatation	ZO-1, VE-cadherin, Laminin, Tubulin, ACE-2, $\alpha$ -1a adrenergic, acetylcholine	<i>In vivo</i> grafts, <i>in vitro</i> models	This study

**Movie S1.** Tensile tests applied on (A) a (bio)printed mono-layered conduit and (B) a mouse *vena cava*. Replayed at 16× speed.

**Movie S2.** Burst pressure tests for (A) a (bio)printed vascular conduits, (B) a mouse *vena cava*, and (C) a mouse aorta. Replayed at 1× speed.

**Movie S3.** Perfusion of RBC suspension into a (bio)printed long mono-layered conduit. Replayed at 1× speed.

**Movie S4.** Demonstration of a bioreactor for permeability experiments. Replayed at 8× speed.

**Movie S5.** Permeability tests applied on (bio)printed vascular conduits in the presence or absence of endothelial cells within the first 10 min. (A) an acellular mono-layered conduit, (B) a mono-layered conduit with confluent HUVECs in the lumen, (C) an acellular dual-layered conduit, (D) a dual-layered conduit with confluent HUAECs in the lumen. Replayed at 8× speed.

**Movie S6.** Anastomose tests of (bio)printed vascular conduits and native blood vessels by perfusing fluorescent beads. (A) a small-sized (bio)printed vascular conduit anastomosed with a mouse aorta on a 3-cm petri dish, (B) a large-size (bio)printed vascular conduit anastomosed with a human popliteal vein on a 10-cm petri dish. Replayed at 1× speed.

## REFERENCES AND NOTES

1. C. Hwa, A. Sebastian, W. C. Aird, Endothelial biomedicine: Its status as an interdisciplinary field, its progress as a basic science, and its translational bench-to-bedside gap. *Endothelium* **12**, 139–151 (2005).
2. S. P. Herbert, D. Y. R. Stainier, Molecular control of endothelial cell behaviour during blood vessel morphogenesis. *Nat. Rev. Mol. Cell Biol.* **12**, 551–564 (2011).
3. W. D. Tucker, Y. Arora, K. Mahajan, *Anatomy, Blood Vessels* (StatPearls Publishing LLC., 2021).
4. S. S. Virani, A. Alonso, H. J. Aparicio, E. J. Benjamin, M. S. Bittencourt, C. W. Callaway, A. P. Carson, A. M. Chamberlain, S. Cheng, F. N. Delling, M. S. V. Elkind, K. R. Evenson, J. F. Ferguson, D. K. Gupta, S. S. Khan, B. M. Kissela, K. L. Knutson, C. D. Lee, T. T. Lewis, J. Liu, M. S. Loop, P. L. Lutsey, J. Ma, J. Mackey, S. S. Martin, D. B. Matchar, M. E. Mussolino, S. D. Navaneethan, A. M. Perak, G. A. Roth, Z. Samad, G. M. Satou, E. B. Schroeder, S. H. Shah, C. M. Shay, A. Stokes, L. B. VanWagner, N. Y. Wang, C. W. Tsao; American Heart Association Council on Epidemiology and Prevention Statistics Committee and Stroke Statistics Subcommittee, Heart disease and stroke statistics-2021 update: A report from the american heart association. *Circulation* **143**, e254–e743 (2021).
5. G. A. Roth, G. A. Mensah, C. O. Johnson, G. Addolorato, E. Ammirati, L. M. Baddour, N. C. Barengo, A. Z. Beaton, E. J. Benjamin, C. P. Benziger, A. Bonny, M. Brauer, M. Brodmann, T. J. Cahill, J. Carapetis, A. L. Catapano, S. S. Chugh, L. T. Cooper, J. Coresh, M. Criqui, N. DeCleene, K. A. Eagle, S. Emmons-Bell, V. L. Feigin, J. Fernández-Solà, G. Fowkes, E. Gakidou, S. M. Grundy, F. J. He, G. Howard, F. Hu, L. Inker, G. Karthikeyan, N. Kassebaum, W. Koroshetz, C. Lavie, D. Lloyd-Jones, H. S. Lu, A. Mirijello, A. M. Temesgen, A. Mokdad, A. E. Moran, P. Muntner, J. Narula, B. Neal, M. Ntsekhe, G. Moraes de Oliveira, C. Otto, M. Owolabi, M. Pratt, S. Rajagopalan, M. Reitsma, A. L. P. Ribeiro, N. Rigotti, A. Rodgers, C. Sable, S. Shakil, K. Sliwa-Hahnle, B. Stark, J. Sundström, P. Timpel, I. M. Tleyjeh, M. Valgimigli, T. Vos, P. K. Whelton, M. Yacoub, L. Zuhlke, C. Murray, V. Fuster, Global Burden of Cardiovascular Diseases and Risk Factors, Global burden of cardiovascular diseases and risk factors, 1990–2019. *J. Am. Coll. Cardiol.* **76**, 2982–3021 (2020).

6. L. D. Hillis, P. K. Smith, J. L. Anderson, J. A. Bittl, C. R. Bridges, J. G. Byrne, J. E. Cigarroa, V. J. DiSesa, L. F. Hiratzka, A. M. Hutter, Jr., M. E. Jessen, E. C. Keeley, S. J. Lahey, R. A. Lange, M. J. London, M. J. Mack, M. R. Patel, J. D. Puskas, J. F. Sabik, O. Selnes, D. M. Shahian, J. C. Trost, M. D. Winniford, A. K. Jacobs, J. L. Anderson, N. Albert, M. A. Creager, S. M. Ettinger, R. A. Guyton, J. L. Halperin, J. S. Hochman, F. G. Kushner, E. M. Ohman, W. Stevenson, C. W. Yancy; American College of Cardiology Foundation/American Heart Association Task Force on Practice Guidelines, 2011 ACCF/AHA guideline for coronary artery bypass graft surgery: Executive summary: A report of the American College of Cardiology Foundation/American Heart Association Task Force on practice guidelines. *J. Thorac. Cardiovasc. Surg.* **143**, 4–34 (2012).
7. I. Ahmed, S. Yandrapalli, *Internal Mammary Artery Bypass* (StatPearls Publishing LLC., 2021).
8. P. Altshuler, P. Nahirniak, N. J. Welle, *Saphenous Vein Grafts* (StatPearls Publishing LLC., 2021).
9. STS data clarifies variables behind coronary artery bypass complication, mortality rates. *Data Strateg. Benchmarks* **2**, 172–174, 161 (1998).
10. A. L. Hawkes, M. Nowak, B. Bidstrup, R. Speare, Outcomes of coronary artery bypass graft surgery. *Vasc. Health Risk Manag.* **2**, 477–484 (2006).
11. B. McNichols, J. R. Spratt, J. George, S. Rizzi, E. W. Manning, K. Park, Coronary artery bypass: Review of surgical techniques and impact on long-term revascularization outcomes. *Cardiol. Ther.* **10**, 89–109 (2021).
12. J. G. Motwani, E. J. Topol, Aortocoronary saphenous vein graft disease. *Circulation* **97**, 916–931 (1998).
13. A. Malinska, Z. Podemska, B. Perek, M. Jemielity, P. Buczkowski, M. Grzymislawska, P. Sujka-Kordowska, M. Nowicki, Preoperative factors predicting saphenous vein graft occlusion in coronary artery bypass grafting: A multivariate analysis. *Histochem. Cell Biol.* **148**, 417–424 (2017).
14. A. Lejay, V. Vento, S. Kuntz, L. Steinmetz, Y. Georg, F. Thaveau, F. Heim, N. Chakfé, Current status on vascular substitutes. *J. Cardiovasc. Surg. (Torino)* **61**, 538–543 (2020).

15. H.-H. Greco Song, R. T. Rumma, C. K. Ozaki, E. R. Edelman, C. S. Chen, Vascular tissue engineering: Progress, challenges, and clinical promise. *Cell Stem Cell* **22**, 340–354 (2018).
16. M. D. Sarker, S. Naghieh, N. K. Sharma, L. Ning, X. Chen, Bioprinting of vascularized tissue scaffolds: Influence of biopolymer, cells, growth factors, and gene delivery. *J. Healthc. Eng.* **2019**, 9156921 (2019).
17. X. Cao, S. Maharjan, R. Ashfaq, J. Shin, Y. S. Zhang, Bioprinting of small-diameter blood vessels. *Engineering* **7**, 832–844 (2021).
18. P. Sasmal, P. Datta, Y. Wu, I. T. Ozbolat, 3D bioprinting for modelling vasculature. *Microphysiol. Syst.* **2**, 9 (2018).
19. Y. S. Zhang, G. Haghighashtiani, T. Hübscher, D. J. Kelly, J. M. Lee, M. Lutolf, M. C. McAlpine, W. Y. Yeong, M. Zenobi-Wong, J. Malda, 3D extrusion bioprinting. *Nat. Rev. Methods Primers* **1**, 75 (2021).
20. D. N. d. Chatinier, K. P. Figler, P. Agrawal, W. Liu, Y. S. Zhang, The potential of microfluidics-enhanced extrusion bioprinting. *Biomicrofluidics* **15**, 041304 (2021).
21. M. Costantini, C. Colosi, W. Świążzkowski, A. Barbetta, Co-axial wet-spinning in 3D bioprinting: State of the art and future perspective of microfluidic integration. *Biofabrication* **11**, 012001 (2019).
22. S. Hong, S. K. Ji, B. Jung, C. Won, C. Hwang, Coaxial bioprinting of cell-laden vascular constructs using a gelatin-tyramine bioink. *Biomater. Sci.* **7**, 4578–4587 (2019).
23. L. Andrique, G. Recher, K. Alessandri, N. Pujol, M. Feyeux, P. Bon, L. Cognet, P. Nassoy, A. Bikfalvi, A model of guided cell self-organization for rapid and spontaneous formation of functional vessels. *Sci. Adv.* **5**, eaau6562 (2019).
24. G. Gao, J. Y. Park, B. S. Kim, J. Jang, D.-W. Cho, Coaxial cell printing of freestanding, perfusable, and functional in vitro vascular models for recapitulation of native vascular endothelium pathophysiology. *Adv. Healthc. Mater.* **7**, 1801102 (2018).

25. G. Gao, W. Park, B. S. Kim, M. Ahn, S. Chae, W.-W. Cho, J. Kim, J. Y. Lee, J. Jang, D.-W. Cho, Construction of a novel in vitro atherosclerotic model from geometry-tunable artery equivalents engineered via in-bath coaxial cell printing. *Adv. Funct. Mater.* **31**, 2008878 (2021).
26. W. Jia, P Selcan Gungor-Ozkerim, Y. S. Zhang, K. Yue, K. Zhu, W. Liu, Q. Pi, B. Byambaa, M. R. Dokmeci, S. R. Shin, A. Khademhosseini, Direct 3D bioprinting of perfusable vascular constructs using a blend bioink. *Biomaterials* **106**, 58–68 (2016).
27. Q. Pi, S. Maharjan, X. Yan, X. Liu, B. Singh, A. M. van Genderen, F. Robledo-Padilla, R. Parra-Saldivar, N. Hu, W. Jia, C. Xu, J. Kang, S. Hassan, H. Cheng, X. Hou, A. Khademhosseini, Y. S. Zhang, Digitally tunable microfluidic bioprinting of multilayered cannular tissues. *Adv. Mat.* **30**, e1706913 (2018).
28. Q. Liang, F. Gao, Z. Zeng, J. Yang, M. Wu, C. Gao, D. Cheng, H. Pan, W. Liu, C. Ruan, Coaxial scale-up printing of diameter-tunable biohybrid hydrogel microtubes with high strength, perfusability, and endothelialization. *Adv. Funct. Mater.* **30**, 2001485 (2020).
29. Y. Zhang, Y. Yu, A. Akkouch, A. Dababneh, F. Dolati, I. T. Ozbolat, In vitro study of directly bioprinted perfusable vasculature conduits. *Biomater. Sci.* **3**, 134–143 (2015).
30. J. P. Gong, Y. Katsuyama, T. Kurokawa, Y. Osada, Double-network hydrogels with extremely high mechanical strength. *Adv. Mat.* **15**, 1155–1158 (2003).
31. X. Zhao, X. Chen, H. Yuk, S. Lin, X. Liu, G. Parada, Soft materials by design: Unconventional polymer networks give extreme properties. *Chem. Rev.* **121**, 4309–4372 (2021).
32. N. Contessi Negrini, A. Angelova Volponi, P. T. Sharpe, A. D. Celiz, Tunable cross-linking and adhesion of gelatin hydrogels via bioorthogonal click chemistry. *ACS Biomater Sci. Eng.* **7**, 4330–4346 (2021).
33. C. W. Yung, L. Q. Wu, J. A. Tullman, G. F. Payne, W. E. Bentley, T. A. Barbari, Transglutaminase crosslinked gelatin as a tissue engineering scaffold. *J. Biomed. Mater. Res. A* **83**, 1039–1046 (2007).
34. J. P. Gong, Why are double network hydrogels so tough? *Soft Matter* **6**, 2583–2590 (2010).

35. O. Chaudhuri, L. Gu, D. Klumpers, M. Darnell, S. A. Bencherif, J. C. Weaver, N. Huebsch, H.-p. Lee, E. Lippens, G. N. Duda, D. J. Mooney, Hydrogels with tunable stress relaxation regulate stem cell fate and activity. *Nat. Mater.* **15**, 326–334 (2016).
36. J. Li, Y. Wu, J. He, Y. Huang, A new insight to the effect of calcium concentration on gelation process and physical properties of alginate films. *J. Mater. Sci.* **51**, 5791–5801 (2016).
37. B. G. Compton, J. A. Lewis, 3D-printing of lightweight cellular composites. *Adv. Mat.* **26**, 5930–5935 (2014).
38. S. A. Ghodbane, N. S. Murthy, M. G. Dunn, J. Kohn, Achieving molecular orientation in thermally extruded 3D printed objects. *Biofabrication* **11**, 045004 (2019).
39. J. L. Drury, R. G. Dennis, D. J. Mooney, The tensile properties of alginate hydrogels. *Biomaterials* **25**, 3187–3199 (2004).
40. S. K. Burke, K. Bingham, E. Moss, D. P. Gottlieb, M. D. Wong, K. S. Bland, F. N. Franano, Recombinant human elastase alters the compliance of atherosclerotic tibial arteries after ex vivo angioplasty. *J. Cardiovasc. Pharmacol.* **67**, 305–311 (2016).
41. J. Gavard, Endothelial permeability and VE-cadherin: A wacky comradeship. *Cell Adh. Migr.* **7**, 455–461 (2013).
42. W. Liu, Z. Zhong, N. Hu, Y. Zhou, L. Maggio, A. K. Miri, A. Fragasso, X. Jin, A. Khademhosseini, Y. S. Zhang, Coaxial extrusion bioprinting of 3D microfibrillar constructs with cell-favorable gelatin methacryloyl microenvironments. *Biofabrication* **10**, 024102 (2018).
43. S. Pashneh-Tala, S. MacNeil, F. Claeysens, The tissue-engineered vascular graft-past, present, and future. *Tissue Eng. Part B Rev.* **22**, 68–100 (2016).
44. “Structure and function of blood vessels”; <https://courses.lumenlearning.com/suny-ap2/chapter/structure-and-function-of-blood-vessels/>.

45. A. Banerjee, M. Arha, S. Choudhary, R. S. Ashton, S. R. Bhatia, D. V. Schaffer, R. S. Kane, The influence of hydrogel modulus on the proliferation and differentiation of encapsulated neural stem cells. *Biomaterials* **30**, 4695–4699 (2009).
46. M. J. Davis, M. A. Hill, Signaling mechanisms underlying the vascular myogenic response. *Physiol. Rev.* **79**, 387–423 , (1999).
47. M. A. Hill, G. A. Meininger, M. J. Davis, I. Laher, Therapeutic potential of pharmacologically targeting arteriolar myogenic tone. *Trends Pharmacol. Sci.* **30**, 363–374 (2009).
48. K. F. Franzen, M. Meusel, J. Engel, T. Röcker, D. Drömann, F. Sayk, Differential effects of Angiotensin-II compared to phenylephrine on arterial stiffness and hemodynamics: A placebo-controlled study in healthy humans. *Cells* **10**, 1108 (2021).
49. H. B. Nguyen, S. Y. Lee, S. H. Park, M. Y. Lee, I. H. Chang, S. C. Myung, Relaxing effect of acetylcholine on phenylephrine-induced contraction of isolated rabbit prostate strips is mediated by neuronal nitric oxide synthase. *Korean J. Urol.* **54**, 333–338 (2013).
50. “COVID-19 dashboard by the Center for Systems Science and Engineering (CSSE) at Johns Hopkins University (JHU)”;  
<https://coronavirus.jhu.edu/map.html>.
51. C. B. Jackson, M. Farzan, B. Chen, H. Choe, Mechanisms of SARS-CoV-2 entry into cells. *Nat. Rev. Mol. Cell Biol.* **23**, 3–20 (2022).
52. K. Katella, “Omicron, delta, alpha, and more: What to know about the coronavirus variants” (Yale Medicine, 2022); [www.yalemedicine.org/news/covid-19-variants-of-concern-omicron](http://www.yalemedicine.org/news/covid-19-variants-of-concern-omicron).
53. S. K. Abrokwa, S. A. Müller, A. Méndez-Brito, J. Hanefeld, C. El Bcheraoui, Recurrent SARS-CoV-2 infections and their potential risk to public health - A systematic review. *PLOS ONE* **16**, e0261221 (2021).
54. R. Rauti, M. Shahoha, Y. Leichtmann-Bardoogo, R. Nasser, E. Paz, R. Tamir, V. Miller, T. Babich, K. Shaked, A. Ehrlich, K. Ioannidis, Y. Nahmias, R. Sharan, U. Ashery, B. M. Maoz, Effect of SARS-CoV-2 proteins on vascular permeability. *eLife* **10**, e69314 (2021).

55. L. C. Barbosa, T. L. Gonçalves, L. Prudencio de Araujo, L. Vieira de Oliveira Rosario, V. P. Ferrer, Endothelial cells and SARS-CoV-2: An intimate relationship. *Vascul. Pharmacol.* **137**, 106829 (2021).
56. COVID-19 and vascular disease. *EBioMedicine* **58**, 102966 (2020).
57. A. J. Pruijssers, A. S. George, A. Schäfer, S. R. Leist, L. E. Gralinski, K. H. Dinno III, B. L. Yount, M. L. Agostini, L. J. Stevens, J. D. Chappell, X. Lu, T. M. Hughes, K. Gully, D. R. Martinez, A. J. Brown, R. L. Graham, J. K. Perry, V. D. Pont, J. Pitts, B. Ma, D. Babusis, E. Murakami, J. Y. Feng, J. P. Bilello, D. P. Porter, T. Cihlar, R. S. Baric, M. R. Denison, T. P. Sheahan, Remdesivir inhibits SARS-CoV-2 in human lung cells and chimeric SARS-CoV expressing the SARS-CoV-2 RNA polymerase in mice. *Cell Rep.* **32**, 107940 (2020).
58. S. Weston, C. M. Coleman, R. Haupt, J. Logue, M. B. Frieman, Broad anti-coronavirus activity of Food and Drug Administration-approved drugs against SARS-CoV-2 *in vitro* and SARS-CoV *in vivo*. *J. Virol.* **94**, e01218–e01220 (2020).
59. C. L. Onweni, Y. S. Zhang, T. Caulfield, C. E. Hopkins, D. L. Fairweather, W. D. Freeman, ACEI/ARB therapy in COVID-19: The double-edged sword of ACE2 and SARS-CoV-2 viral docking. *Crit. Care* **24**, 475 (2020).
60. A. G. Harrison, T. Lin, P. Wang, Mechanisms of SARS-CoV-2 transmission and pathogenesis. *Trends Immunol.* **41**, 1100–1115 (2020).
61. J. Gong, C. C. L. Schuurmans, A. M. van Genderen, X. Cao, W. Li, F. Cheng, J. J. He, A. López, V. Huerta, J. Manríquez, R. Li, H. Li, C. Delavaux, S. Sebastian, P. E. Capendale, H. Wang, J. Xie, M. Yu, R. Masereeuw, T. Vermonden, Y. S. Zhang, Complexation-induced resolution enhancement of 3D-printed hydrogel constructs. *Nat. Commun.* **11**, 1267 (2020).
62. S. Maharjan, J. Alva, C. Cámara, A. G. Rubio, D. Hernández, C. Delavaux, E. Correa, M. D. Romo, D. Bonilla, M. L. Santiago, W. Li, F. Cheng, G. Ying, Y. S. Zhang, Symbiotic photosynthetic oxygenation within 3D-bioprinted vascularized tissues. *Matter* **4**, 217–240 (2021).

63. H. Ravanbakhsh, Z. Luo, X. Zhang, S. Maharjan, H. S. Mirkarimi, G. Tang, C. Chávez-Madero, L. Mongeau, Y. S. Zhang, Freeform cell-laden cryobioprinting for shelf-ready tissue fabrication and storage. *Matter* **5**, 573–593 (2022).
64. H. Han, Y. Park, Y.-M. Choi, U. Yong, B. Kang, W. Shin, S. Min, H. J. Kim, J. Jang, A bioprinted tubular intestine model using a colon-specific extracellular matrix bioink. *Adv. Healthc. Mater.* **11**, 2101768 (2022).
65. C. Xiang, Z. Wang, C. Yang, X. Yao, Y. Wang, Z. Suo, Stretchable and fatigue-resistant materials. *Mater. Today* **34**, 7–16 (2020).
66. S. Massa, M. A. Sakr, J. Seo, P. Bandaru, A. Arneri, S. Bersini, E. Zare-Eelanjegh, E. Jalilian, B.-H. Cha, S. Antona, A. Enrico, Y. Gao, S. Hassan, J. P. Acevedo, M. R. Dokmeci, Y. S. Zhang, A. Khademhosseini, S. R. Shin, Bioprinted 3D vascularized tissue model for drug toxicity analysis. *Biomicrofluidics* **11**, 044109 (2017).
67. D. B. Kolesky, K. A. Homan, M. A. Skylar-Scott, J. A. Lewis, Three-dimensional bioprinting of thick vascularized tissues. *Proc. Natl. Acad. Sci. U.S.A.* **113**, 3179–3184 (2016).
68. D. Wang, W. Chen, Indocyanine green angiography for continuously monitoring blood flow changes and predicting perfusion of deep inferior epigastric perforator flap in rats. *J. Invest. Surg.* **34**, 393–400 (2021).
69. D. Huang, T. Liu, J. Liao, S. Maharjan, X. Xie, M. Pérez, I. Anaya, S. Wang, A. Tirado Mayer, Z. Kang, W. Kong, V. L. Mainardi, C. E. Garciamendez-Mijares, G. García Martínez, M. Moretti, W. Zhang, Z. Gu, A. M. Ghaemmaghami, Y. S. Zhang, Reversed-engineered human alveolar lung-on-a-chip model. *Proc. Natl. Acad. Sci. U.S.A.* **118**, e2016146118 (2021).
70. Q. Gao, Y. He, J.-Z. Fu, A. Liu, L. Ma, Coaxial nozzle-assisted 3D bioprinting with built-in microchannels for nutrients delivery. *Biomaterials* **61**, 203–215 (2015).
71. G. Gao, J. H. Lee, J. Jang, D. H. Lee, J.-S. Kong, B. S. Kim, Y.-J. Choi, W. B. Jang, Y. J. Hong, S.-M. Kwon, D.-W. Cho, Tissue engineered bio-blood-vessels constructed using a tissue-specific bioink and

- 3D coaxial cell printing technique: A novel therapy for ischemic disease. *Adv. Funct. Mater.* **27**, 1700798 (2017).
72. G. Gao, H. Kim, B. S. Kim, J. S. Kong, J. Y. Lee, B. W. Park, S. Chae, J. Kim, K. Ban, J. Jang, H.-J. Park, D.-W. Cho, Tissue-engineering of vascular grafts containing endothelium and smooth-muscle using triple-coaxial cell printing. *Appl. Phys. Rev.* **6**, 041402 (2019).
73. S. C. Millik, A. M. Dostie, D. G. Karis, P. T. Smith, M. McKenna, N. Chan, C. D. Curtis, E. Nance, A. B. Theberge, A. Nelson, 3D printed coaxial nozzles for the extrusion of hydrogel tubes toward modeling vascular endothelium. *Biofabrication* **11**, 045009 (2019).
74. L. Shao, Q. Gao, C. Xie, J. Fu, M. Xiang, Y. He, Directly coaxial 3D bioprinting of large-scale vascularized tissue constructs. *Biofabrication* **12**, 035014 (2020).